THESIS FOR THE DEGREE OF DOCTOR OF PHILOSOPHY

# Human Body Model Morphing for Assessment of Crash Rib Fracture Risk for the Population of Car Occupants

KARL-JOHAN M. LARSSON

Department of Mechanics and Maritime Sciences
Division of Vehicle Safety
Injury Prevention
CHALMERS UNIVERSITY OF TECHNOLOGY
Gothenburg, Sweden 2023

Human Body Model Morphing for Assessment of Crash Rib Fracture Risk for the Population of Car Occupants

KARL-JOHAN M. LARSSON
ISBN 978-91-7905-836-4



Doktorsavhandlingar vid Chalmers tekniska högskola
Ny serie nr 5302
ISSN 0346-718X

Department of Mechanics and Maritime Sciences
Division of Vehicle Safety
Injury Prevention
Chalmers University of Technology

SE-412 96 Göteborg

Sweden

Telephone: + 46 (0)31-772 1000

Chalmers Reproservice
Göteborg, Sweden 2023-05

Human Body Model Morphing for Assessment of Crash Rib Fracture Risk for the Population of Car Occupants
KARL-JOHAN M. LARSSON

# Abstract

Fractured ribs are prevalent injury outcomes for vehicle occupants involved in crashes. Sex, age, and anthropometry of an occupant influences the risk to sustain rib fractures. The SAFER human body model (SHBM) represents an average sized male and includes a detailed ribcage model that has been validated for prediction of rib fracture risk in virtual crash simulations. Developments in parametric morphing of human body models have enabled re-shaping the SHBM to represent a wide range of body sizes for both adult males and females which can influence kinematic and injury risk predictions. The aim for this thesis was to enable the assessment of crash kinematics and rib fracture risk for the population of occupants by morphing the SHBM. Research was performed within objectives that included: providing a definition of the occupant population, creating morphed versions of the SHBM (MHBMs) and validating MHBM crash kinematic and rib fracture risk predictions within the defined population, develop a method to efficiently compute rib fracture risk across the population, and investigate factors beyond morphing that influences MHBM rib fracture risk predictions.

The population definition includes 90 % of the U.S.-population in terms of male and female height and weight variability. For validation, parametric morphing was used to create MHBMs geometrically matching age, sex, height, and weight of 22 human subjects in previous crash tests. Rib fracture risk and kinematic predictions from MHBMs were validated by comparison to test results and MHBMs showed good correlation for kinematics and had acceptable utility to predict rib fracture outcomes. However, the rib fracture risk for the most vulnerable, predominantly older, occupants was underestimated. One reason can be rib cortical bone microstructural defects, that are not represented by current SHBM rib material modeling.

To compute population rib fracture risk in crashes, a metamodeling method based on 25 differently sized MHBMs of each sex was recommended. Using this metamodeling, method it was also identified that seven selected MHBMs of each sex can be used to predict the population risk across two specific crash scenarios. This indicates a possibility to identify a small family of MHBMs that are generally representative of population rib fracture risk in future work.

For further improving rib fracture risk predictions, a new rib fracture risk function was developed based on human rib test results. The new function is more sensitive to age compared to previous risk functions. Additionally, it was identified that the individual variability in rib cross-sectional width, as well as cortical bone thickness and material properties all substantially influence rib fracture risk predictions. Including the individual variability in these influential parameters in MHBM models will improve the capability of MHBMs to predict the rib fracture risk variability that exists in the population of occupants independently of sex, height, and weight.

It is concluded that MHBMs representing geometrical shape trends due to height, weight and sex, and individual rib local variability can be used to assess kinematics and rib fracture risk for wide range of males and females of different sizes. However, more research is needed to accurately predict the risk for the most vulnerable, predominantly older occupants.

**Keywords**: human body model, SAFER HBM, rib fracture risk, morphing, vehicle safety, crash

# List of Appended Publications

This thesis is based on the work contained in the following papers, referred to by roman numerals in the main text. Contributions of Larsson K.-J. listed using CRediT.

I. Larsson K.-J., Pipkorn B., Iraeus J., Forman J., Hu J. (2022), Evaluation of a Diverse Population of Morphed Human Body Models for Prediction of Vehicle Occupant Crash Kinematics, *Computer Methods in Biomechanics and Biomedical Engineering* 25(10): 1125-1155.
Contributions: Conceptualization, Data Curation, Formal Analysis, Methodology, Visualization, Validation, Writing – Original draft.

II. Larsson K.-J., Östh J., Iraeus J., Pipkorn B., (2023), A First Step Towards a Family of Morphed Human Body Models Enabling Prediction of Population Injury Outcomes, *Manuscript submitted to Accident Analysis and Prevention.*
Contributions: Conceptualization, Formal Analysis, Methodology, Software, Validation, Visualization, Writing – Original draft

III. Larsson K.-J., Blennow A., Iraeus J., Pipkorn B., Lubbe N. (2021), Rib Cortical Bone Fracture Risk as a Function of Age and Rib Strain: Updated Injury Prediction Using Finite Element Human Body Models, *Frontiers in Bioengineering and Biotechnology* 9:677768: 1-12.
Contributions: Conceptualization, Methodology, Project Administration, Validation, Writing – Original draft

IV. Larsson K.-J., Iraeus J., Holcombe S., Pipkorn B. (2023), Influences of human thorax variability on population rib fracture risk prediction using human body models, *Frontiers in Bioengineering and Biotechnology* 11:1154272: 1-14.
Contributions: Conceptualization, Data Curation, Formal Analysis, Methodology, Software, Validation, Visualization, Writing – Original draft

# Contents


Abstract ..... I
List of Appended Publications ..... II
Contents ..... III
Acknowledgements ..... V
Abbreviations ..... VI
1 Introduction ..... 1
1.1 Occupant Safety Evaluation ..... 1
1.1.1 Anthropomorphic Test Devices ..... 2
1.1.2 Virtual Crash Testing ..... 3
1.1.3 Virtual Human Body Models ..... 3
1.1.4 Representing occupant variability through HBM morphing ..... 4
1.2 Aim and Objectives ..... 5
1.3 Outline of Thesis ..... 5
2 Background and Methods ..... 6
2.1 Thoracic Anatomy, Variability, and Injuries ..... 6
2.1.1 Thoracic Variability ..... 7
2.1.2 Thoracic Injuries ..... 7
2.2 SHBM Rib Modeling ..... 8
2.3 Statistical Methods ..... 9
2.3.1 Principal Component Analysis ..... 9
2.3.2 Regression modelling ..... 10
2.3.3 Classification and risk functions ..... 12
2.4 HBM Validation ..... 13
2.5 SHBM Rib Fracture Risk Prediction ..... 13
2.6 Parametric HBM Morphing ..... 14
2.7 Model Sensitivity Analysis ..... 17
3 Objective I: Define the Target Population ..... 18
4 Objective II: MHBM Validation ..... 19
4.1 Summary of Paper I: Validation of MHBM crash Kinematics ..... 19
4.2 Re-validation of MHBMs based on SHBM v.10 ..... 21
4.3 Validation of MHBM Rib Fracture Risk Predictions ..... 23
5 Objective III: Population Rib Fracture Risk ..... 26
5.1 Summary of Paper II ..... 26
6 Objective IV: Additional Parameters ..... 28
6.1 Summary of Paper III ..... 28

6.2 Summary of Paper IV ..... 29
7 Discussion and Future Work ..... 32
7.1 Definition of target population ..... 32
7.2 Validation of MHBM Kinematic Predictions ..... 33
7.3 Validation of MHBM Rib Fracture Risk Predictions ..... 35
7.4 Population Rib Fracture Risk ..... 37
7.5 Additional Influential Parameters ..... 39
7.6 Applications ..... 40
7.7 Limitations ..... 40
8 Conclusions ..... 42
9 References ..... 43

# Acknowledgements

The work performed for this thesis has been performed at the Injury Prevention Research group, Division of Vehicle Safety, Chalmers University of Technology, at Autoliv Development AB, and at SAFER-the Vehicle and Traffic Safety Centre at Chalmers University during 2018–2023. Supervision was provided by Adj. Professor Bengt Pipkorn (main supervisor), Dr. Johan Iraeus (assistant supervisor), with additional supervision from Professor Mats Svensson (examiner) and Adj. Professor Lotta Jakobsson.

The work has been conducted within two projects, that both have received funding from FFI – Strategic Vehicle Research and Innovation, by Vinnova, the Swedish Energy Agency, the Swedish Transport Administration, the Swedish vehicle industry. The first project (2017-2020) was Assessment of Passenger Safety in Future Cars (swe: Passagerarsäkerhetsutvärdering i framtida bilar). The second project (2020 - 2023) was Car Passenger Safety – to the next level (swe: Passagerarsäkerhet i bil – till nästa nivå). In both projects, partners were Autoliv Development, Chalmers University and Volvo Cars.

The human body model morphing method, www.humanshape.org, used within this thesis has been implemented for the SAFER human body model in cooperation with University of Michigan Transportation Research Institute.

Performing the work and studies for this thesis would not have been possible without the support and guidance provided from several individuals. Mats Svensson, Lotta Jakobsson, and especially Bengt Pipkorn and Johan Iraeus have spent a lot of time and energy to provide me with support and feedback and I'm grateful for every minute. I hope we can have many more interesting discussions in the future.

I want to thank Chalmers staff for support and fellow PhD students at the Injury Prevention Group, I Putu Alit Putra, Erik Brynskog, Alexandros Leledakis, Emma Larsson, Jonny Genzel, and Linus Lundin for support and interesting discussions.

I'm also grateful to my employer Autoliv Research, for enabling and supporting me in my education. It is very stimulating to perform research in this environment, closely connected to real-world needs and applications. Thanks to all my colleagues, and special thanks to my manager Nils Lübbe, who has provided me with excellent advice and feedback.

I also want to thank my friends and family, especially Sebastian Jobjörnsson for endless discussions about everything and nothing.

Last, but not least, I want to thank my wonderful girls Lina and Li for putting up with me.

Göteborg 2023-05

KARL-JOHAN M. LARSSON

# Abbreviations

| | |
|---|---|
| ATD | Anthropomorphic test device (commonly known as crash test dummy) |
| AUC | Area under the receiver operating characteristic curve |
| BMI | Body mass index (Weight/Height$^2$, [kg/m$^2$]) |
| CT | Computed tomography |
| FE | Finite element |
| GPR | Gaussian Process Regression |
| HBM | Human body model |
| MHBM | Morphed human body model |
| NFR2+ | Risk of two or more fractured ribs |
| NHANES | National Health and Nutrition Examination Survey |
| PC | Principal component |
| PCA | Principal component analysis |
| PMHS | Post mortem human subject |
| ROC | Receiver operator characteristics curve |
| SD | Standard deviation |
| SHBM | SAFER human body model |
| UMTRI | University of Michigan Transportation Research Institute |

# 1 Introduction

Vehicle occupants represent nearly a third of the 1.35 million yearly deaths from road traffic crashes (World Health Organization 2018). Among severe occupant injuries, fractured ribs is one of the most common (Welsh and Lenard 2001; Forman et al., 2019). As the ribcage forms a protective shell around the vital organs of the thorax, rib fractures are associated with an increased risk of fatality, especially for older occupants (>64 years) (Kent et al., 2008), and as few as three (or more) rib fractures has been identified as an independent and significant risk factor for mortality (Battle et al., 2012).

Moreover, analysis of crash injury databases has indicated that the risk to sustain rib fractures and thoracic injuries, as well as other injuries, is not the same for all occupants in the population. Increasing body mass index (BMI, weight/height$^2$ [kg/m$^2$]) has been associated with increasing thoracic injury risk (Carter et al., 2014; Pal et al., 2014; Forman et al., 2019). Specifically, a non-linear trend of rib fracture risk with BMI has been reported, with both low and high BMI occupants showing increased rib fracture risk (Forman and McMurry 2018). When comparing males to females, several studies have reported an increased thoracic and rib fracture injury risk for females (Welsh and Lenard 2001; Bose et al., 2011; Carter et al., 2014; Forman et al., 2019; Ryan and Knodler 2022). If the increased female injury risks are due to physiological differences between males and females or due to that females tend to drive different cars and therefore tend to crash differently has been questioned (Brumbelow and Jermakian 2022). Additionally, occupant age influences rib fracture risk. Increasing occupant age increases rib fracture and thoracic injury risk (Brumbelow 2019; Forman et al., 2019) and age has been described as a greater driver for injury risk than both BMI and sex (Carter et al., 2014).

Traditionally, the population of adult vehicle occupants has been represented by three standard sizes of anthropomorphic test devices (ATDs, i.e., crash test dummies) in most crash safety evaluations. Three fixed sizes have a limited ability to explore the effects of male and female body size variations on crash injury outcome. Newer cars, mainly developed using ATD-based crash testing, have reduced risks for many occupant injuries (Forman et al., 2019; Kullgren et al., 2020). However, rib fracture risk remains high in newer cars (model year > 2009), is still increasing with age and BMI, and remains increased for females (Forman et al., 2019). A possibly contributing factor for the remaining rib fracture risk can be that ATD-estimated chest injury risks from crash testing correlates poorly with real-world crash thoracic injury outcomes (Brumbelow 2020; Brumbelow et al., 2022).

The variation in rib fracture injury risks for different occupants, the limited capability of ATD-based chest injury evaluation, and the high rib fracture risk for occupants even in newer cars demonstrates a need for improved rib fracture risk assessment for the population of occupants, which is the motivation behind the research performed for this thesis. Improved rib fracture risk assessments for the population of occupants can enable development of improved safety systems, with a reduced injury and fatality risk for all occupants.

## 1.1 Occupant Safety Evaluation

During development, vehicle crash safety is evaluated by crash testing, both physically and virtually, using mathematical modeling. To estimate the occupant injury risk in crash tests, occupant substitutes are used. While manufacturers can

choose crash scenarios to evaluate, there are also specific physical crash tests mandated in regulations, such as the United Nations Economic Commission for Europe regulation (European Union), China National Standards (China), and Federal Motor Vehicle Safety Standards (United States). Additionally, organizations that provide publicly available crash safety ratings to promote a high level of safety, such as New Car Assessment Programs (NCAPs) use specific physical test scenarios for occupant safety evaluations. Test specifications includes specific crash scenarios and which ATDs to use as occupant substitute. Common scenarios include frontal and side crashes, impacting the front and the side of the car, respectively.

### 1.1.1 Anthropomorphic Test Devices

ATDs are mechanical representations of humans that can measure forces, moments, accelerations, and deformations in different body regions. The measurements are related to injuries by injury risk functions, mathematically linking physical measurements to a statistical risk of injury, such as chest injury risk. As ATDs are measurement equipment that should be able to reproduce the same measurements in repeated crash tests, they have a mechanically robust construction representing a simplified anatomy that can withstand the forces and wear of repeated crash testing. Common simplifications include representing the ribcage with a few metal ribs and a simplified spine model with a reduced number of joints. ATDs are constructed, instrumented, and validated for estimating injury risks in specific impact directions, which means that different ATDs are used for different impact scenarios, such as the Hybrid III and THOR ATDs for frontal impacts, and the EuroSID-2 and WorldSID ATDs for side impacts.

ATDs used to represent the adult occupant population in regulatory and rating crash tests exists in three standard sizes. They represent a 5$^{th}$ percentile (small size) female, a 50$^{th}$ percentile (average size) male, and a 95$^{th}$ percentile (large size) male. Additionally, a 50$^{th}$ percentile female ATD size was suggested, but was removed from the final selection due to lack of funding (Schneider et al., 1983). The percentiles refer to specific heights and weights in distributions measured from the 1970s U.S. population, which were available at the time the ATD anthropometric specifications were set (Schneider et al., 1983). Since then, population weight has increased in the U.S. and around the world (NCD Risk Factor Collaboration et al., 2016). When compared to 2005-2008 U.S. population data, the male 50$^{th}$ and 95$^{th}$ weights corresponded to the 33$^{rd}$ and 81$^{st}$ percentiles of male weights, respectively, while the female 5$^{th}$ corresponded to the 3$^{rd}$ percentile of female weights (Reed and Rupp 2013). This means that 97 % of U.S. females have higher body weights than what is specified for female ATDs and that two-thirds of adult U.S. males are heavier than the average male specification. Too low body weights of ATDs means that the overall kinetic energy represented by the ATDs in crash tests is too low, due to a lack of overall mass. The U.S. population height distributions have not changed as substantially as weight and the ATD sizes represent the 6$^{th}$ (small female ATD), 45$^{th}$ (average male ATD) and 91$^{st}$ (large male ATD) percentiles of their respective U.S. height distributions (Reed and Rupp 2013). The low weights of the average and large male ATDs therefore corresponds to representing lower BMIs, than their counterparts in the contemporary U.S. population, which influences the representation of seatbelt fit (Reed et al., 2013). Increasing BMI is related to an increased layer of soft tissues between the lap-portion of the belt and the pelvis, which allows for more forward excursion of the pelvis before substantial restraint forces can be applied, changing overall excursion kinematics (body displacements relative to the car) of the occupants (Kent et al., 2010; Reed et al., 2013).

### 1.1.2 Virtual Crash Testing

Virtual crash testing is commonly used during the vehicle and safety system development phase, as it reduces the need for physical prototypes, and thus speeds up the development process. Further, it enables studying variations in design parameters and crash conditions in a controlled manner. The car safety rating organization Euro NCAP has communicated its intentions to complement its physical crash testing program for occupant safety with virtual crash testing to include variations in crash conditions, seat position, and occupant substitutes (Euro NCAP 2022).

In virtual crash tests, the vehicle structures, safety systems, occupant substitutes, and crash boundary conditions are represented by mathematical models based on physics. The modelling results in systems of differential equations for which analytical solutions exists only for a very limited number of cases, and therefore numerical methods are used. Typically, commercially available software are used to develop models and to set up and solve the equations using computers. Common modeling strategies in virtual crash testing can broadly be divided into multi-body and finite element (FE) modeling. In multi-body modeling, rigid and flexible bodies, connected by various joint types, are used to construct the models (Wismans et al., 2005). In FE, geometrical bodies are discretized into a finite number of elements interconnected at nodes. The collection of elements and nodes is referred to as a mesh. Appropriate constitutive properties and masses are assigned to the elements to represent different materials, and the relative motions of the nodes are used to calculate strain and stress in the elements. The advantage of the multi-body method is that it often results in much shorter computational times. On the other hand, while being more time-consuming, the FE method facilitates the calculation of detailed deformations of parts of arbitrary shapes and material failure due to e.g., stress or strain-based criteria. Hybrid approaches, i.e., both FE and multi-body modelling present in the virtual crash simulation, are possible.

### 1.1.3 Virtual Human Body Models

In virtual crash testing ATD models, as well as human body models (HBMs) are used. A distinction between ATD models and HBMs is that an ATD model represents a corresponding physical ATD, while HBMs aim to represent humans.

Mathematical models for evaluating the human response in crash loading, including models of specific body parts and the whole human body, have been used since the 1960s, and the level of detail has increased over time (Wismans et al., 2005; Yang et al., 2006). HBMs can model the human anatomy at a greater level of detail than ATDs, for example by including anatomical joints and all ribs of the ribcage and can represent differently sized occupants (Wismans et al., 2005). FE-HBMs with detailed representation of human anatomy and materials have the potential to evaluate injury at the tissue level by calculating physical quantities related to material failure, such as stress, strain, and pressure. Representing the human anatomy and evaluating the injury at the tissue level can allow for a more detailed understanding of the injury mechanism, when compared to an overall body region risk as estimated by ATDs.

Difficulties related to the design of detailed FE-HBMs includes acquiring detailed three-dimensional geometric descriptions of both external and internal geometry of the human body, creating high quality FE-meshes of the part geometries, obtaining and assigning constitutive and material properties, and defining boundary conditions such as contacts and connections between the various parts.

Contemporary FE-HBMs used as adult occupant substitutes in virtual crash testing include the Total Human Model for Safety (THUMS) (Shigeta et al., 2009), Global Human Body Models Consortium (GHBMC) (Gayzik et al., 2012), VIVA+ (John et al., 2022) and SAFER HBM (SHBM) (Pipkorn et al., 2021). These HBMs have detailed ribcage models representing all individual ribs. The thoracic and ribcage geometry of THUMS v.4 (Shigeta et al., 2009) and the GHBMC M50 (Gayzik et al., 2012) are based on medical scanning of individual male subjects that matched the average male ATD size. The VIVA+ and SHBM ribcage geometries are based on statistical shape models for the ribs and sternum (Shi et al., 2014; Weaver, Schoell, Nguyen, et al., 2014; Iraeus et al., 2020; John et al., 2022). The SHBM (v.9) was validated for rib strain (Iraeus and Pipkorn 2019) and strain-based rib fracture risk predictions in various impact scenarios (Pipkorn et al., 2019) and thus has the potential to provide insights into rib fracture injury mechanisms in virtual occupant safety evaluations.

The THUMS and GHBMC HBMs exist in versions representing the small female, as well as the average and large male ATD sizes. The VIVA+ HBMs represent the proposed 50$^{th}$ percentile female ATD and the average male ATD sizes. The SHBM represents the average male ATD size. As such, these HBMs cannot be used directly to predict how variations in height, weight, and age for both sexes influence the injury outcome beyond the pre-specified sizes.

### 1.1.4 Representing occupant variability through HBM morphing

An approach used to modify the anthropometry of FE-HBMs is mesh morphing, where the FE-mesh of an HBM is re-shaped by adjusting the nodal coordinates, such that the morphed HBM (MHBM) represents another body shape. As an example, the large male GHBMC was created by morphing the average male model (Vavalle et al., 2014). In this process, the external and internal geometry from an individual matching the large male specifications were collected. On this geometry, target landmarks were defined. Corresponding source landmarks, each at corresponding (homologous) anatomical locations were defined on the GHBMC average male HBM. The node coordinates describing the average male model were then interpolated to new locations describing the large male geometry using a mapping defined by the source and target landmarks (Vavalle et al., 2014). By utilizing mesh morphing, only new geometrical data and landmarking were needed to define the large male GHBMC. Thus, much of the work required to create the initial GHBMC average male model, such as meshing, assigning material properties, and creating contact and boundary conditions between parts, was avoided, reducing development time needed to obtain an HBM representing an alternative anthropometry.

The University of Michigan Transportation Research Institute (UMTRI) developed a parametric HBM morphing method that utilizes statistical human shape models to describe the morphing target landmarks for a population (Hwang, Hallman, et al., 2016; Hwang, Hu, et al., 2016). This circumvents the need to obtain new geometrical data for every target size. The statistical shape models used in parametric HBM morphing describe the geometry of the body surface, pelvis, femurs, tibiae, and ribcage as functions of input parameters defining targeted age, sex, height, and weight. Once homologous landmarks on the statistical shape models and corresponding parts in an HBM have been defined, mesh morphing can be used to create HBMs geometrically representing a wide range of male and female occupant sizes of different ages.

The ribcage shape model used in the parametric HBM morphing method represents trends in rib cross-sections as well as overall ribcage geometry due to sex, age, height and weight (Wang et al., 2016). Therefore, parametric HBM morphing of the SHBM appears to be a promising method to provide rib fracture risk predictions for the population of occupants.

## 1.2 Aim and Objectives

The overall aim of this thesis is to enable time efficient assessment of kinematics and rib fracture risk in crashes for the population of adult car occupants in virtual crash testing through parametric HBM morphing.

To fulfill the aim, three main objectives have been defined:

**Objective I.** Define the target population
Determine ranges for parametric HBM morphing targets that are representative of the population of car occupants.

**Objective II.** MHBM validation
Using the parametric HBM morphing method, develop and validate MHBMs representing the population for prediction of crash kinematics (Paper I) and rib fracture risk.

**Objective III.** Population rib fracture risk
Develop a method to predict population rib fracture risk and provide recommendations of how many and which MHBMs to use to represent the population variability in rib fracture risk due to sex, height, and weight variability (Paper II).

**Objective IV.** Additional parameters
Determine factors, beyond those considered in the parametric HBM morphing method, that influence the rib fracture risk predictions for the population (Papers III and IV).

## 1.3 Outline of Thesis

Chapter 2, Background and Methods, provides additional background information about thoracic anatomy and injuries, and the rib modelling in the SHBM. Further, methods used for the thesis work are introduced and described.

Chapters 3 to 6 describes research and results and summarizes papers for each of Objectives I-IV.

A discussion, including recommendations for future work is given in Chapter 7, and conclusions are presented in Chapter 8.

# 2 Background and Methods

This chapter covers information on thoracic anatomy, thoracic injuries, and SHBM rib modelling. This is followed by introducing and describing methods used within the thesis, which includes brief descriptions of statistical methods used, the SHBM validation, SHBM rib fracture risk prediction, the parametric HBM morphing, and variance-based sensitivity analysis.

## 2.1 Thoracic Anatomy, Variability, and Injuries

The thorax is the region between abdomen and the neck and broadly consists of its superficial structures, the thoracic wall, and the thoracic cavity. Superficial structures include skin, breasts, adipose (fat) tissue, and muscles (Kudzinskas and Callahan 2022). The thoracic wall consists of the thoracic spine (twelve thoracic vertebrae and intervertebral discs), twelve pairs of ribs, costal cartilage, sternum (breastbone) and muscles used for respiration (breathing). The thoracic wall provides attachment points for muscles of the abdomen, back, shoulders and upper arms and protects the thoracic cavity (Hussain and Burns 2022). The thoracic cavity is bounded by the thoracic wall, the root of the neck and the diaphragm and contains as major organs the lungs, the heart, and the great blood vessels. The thoracic cavity consists of three compartments: the left and right pleura containing the lungs and the mediastinum containing the heart and great blood vessels (Kudzinskas and Callahan 2022).

The ribs are consecutively numbered by levels between one and twelve, with the first rib level being the most superior, closest to the neck. The ribs are flat bones that articulate with the thoracic spine and curves around the thoracic cavity. Ribs one through seven connects directly to the sternum via their own costal cartilages. Ribs eight to ten connects to the cartilage of the ribs above them, and ribs eleven and twelve are floating, shorter ribs, that do not connect to the sternum. The ribs are additionally interconnected through three layers of intercostal muscles between each rib level, Figure 1.

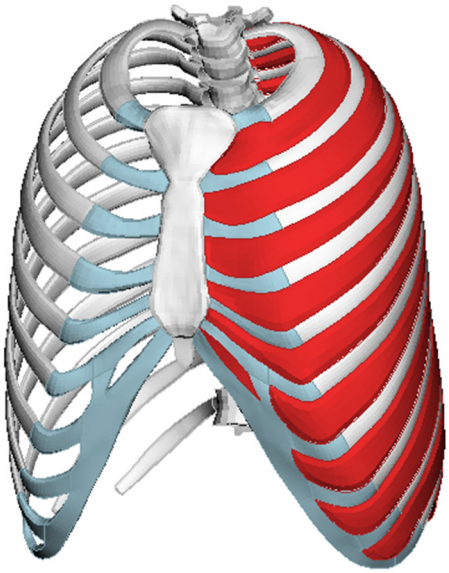

*Figure 1. Thoracic spine, ribs, sternum, costal cartilage, and intercostal muscles (only shown on left-hand side) from the SHBM model.*

The overall cross-sectional shape of the ribs varies between rib levels and along the length of each rib. Each rib consists of two types of bone: a hard, dense outer layer

called cortical bone, and an inner core of softer trabecular, or cancellous, bone, containing the bone marrow. The thickness of the cortical bone varies along and around the ribs, and it is generally greater at the pleural side (inside, towards the thoracic cavity) than on the cutaneous side (outside, towards the skin), and thinner at the superior and inferior edges, with an overall reduced thickness towards the sternal end of the ribs (Mohr et al., 2007; Choi and Kwak 2011; Holcombe and Derstine 2022).

### 2.1.1 Thoracic Variability

In terms of overall ribcage and rib geometry, several studies have identified a substantial individual variability in geometry. However, some statistically significant trends have been identified. One such trend is that the ribs tend to become increasingly more horizontally angled with ageing (Kent et al., 2005; Gayzik et al., 2008; Shi et al., 2014; Weaver, Schoell, and Stitzel 2014; Holcombe et al., 2017). Additionally, a strong trend of increasing rib angles have been identified for increasing body weight and BMI (Kent et al., 2005; Shi et al., 2014; Holcombe et al., 2017). Male ribcages, overall, are wider and deeper than female ribcages (Weaver, Schoell, and Stitzel 2014) and also after accounting for height, weight and age, the rib end-to-end span length is greater in males (Holcombe et al., 2017). Overall, increasing height increases the rib span length for both males and females (Holcombe et al., 2017).

For rib cross-sectional dimensions, males, on average, have overall larger rib cross-sectional areas than females (Shi et al., 2014) and larger area moment of inertia (Holcombe et al., 2019). The thickness of the rib cortical bone has been identified to be similar for young adult males and females, but due to a larger rate of age related bone thinning for females, they have, on average, thinner rib cortical bone than males, from 55 years and older (Holcombe and Derstine 2022).

Substantial individual variability has been identified also in material mechanical properties, which is typical for biological tissues (Cook et al., 2014). Variability in material properties have been identified in the rib cortical and trabecular bone, and in the costal cartilage (Forman et al., 2010; Katzenberger et al., 2020; Kemper et al., 2020; Velázquez-Ameijide et al., 2021). For the rib cortical bone, material properties, such as Young's modulus, yield stress and failure strain, tend to decrease with increasing age (Katzenberger et al., 2020; Velázquez-Ameijide et al., 2021).

### 2.1.2 Thoracic Injuries

Traumatic thoracic injuries are generally divided into blunt and penetrating, based on the cause of the injury. Penetrating injures pierces the tissue, and common mechanisms are for example cuts and gunshots (Dogrul et al., 2020; Edgecombe et al., 2022). They are rare among car crash injuries and are therefore not considered further in the thesis. Blunt chest trauma is most commonly caused by traffic crashes (Sirmali et al., 2003; Edgecombe et al., 2022), but also by falls and workplace accidents. Mortality from blunt chest trauma is due to the disruption of respiration or blood circulation or both. It is common that blunt chest trauma cause multiple simultaneous injuries (Edgecombe et al., 2022), and that patients initially diagnosed with only rib fractures develop later complications due to associated lung and pleural injuries (Sirmali et al., 2003; Karadayi et al., 2011).

The most common blunt chest trauma from traffic crashes involve chest wall injury, followed by lung injuries, pleural and mediastinal injuries, and cardiac or vascular injuries (Benhamed et al., 2022). Among chest wall injuries, rib fractures are the most

frequent, followed by sternal fracture (Benhamed et al., 2022). A type of severe rib fracture injury is called flail chest, in which three or more consecutive ribs are broken in two parts, causing a segment of the chest wall to become disconnected (Dogrul et al., 2020). This causes reduced respiratory function, and is associated with pulmonary contusion and pneumo-/hemothorax (Dogrul et al., 2020). The most common lung injury is pulmonary contusion, which is bruising of the lung tissue, that can be caused by compression or by shockwaves in the tissue. Lung contusion can be present without any apparent chest wall injuries. The most common pleural injuries are pneumothorax and hemothorax, in which air (pneumo) or blood (hemo) are present in the pleural space, compromising lung function.
Pneumo-/hemothorax and lung contusion has been associated with the number of rib fractures, as in Liman et al., (2003) where 7 % of trauma patients without rib fractures, 25 % with one to two, and 82 % with more than two rib fractures were diagnosed with pneumo-/hemothorax. Karadayi et al., (2011) identified pneumo-/hemothorax or lung contusion in 30% of patients with one rib fracture, in 25 % with two, and in 76 % of trauma patients with three or more rib fractures.

## 2.2 SHBM Rib Modeling

The SHBM has a ribcage model representing all 24 ribs, sternum, costal cartilage, intercostal muscle, and the thoracic spine, Figure 1. The development of the ribs is presented in (Iraeus et al., 2020). Briefly, the ribs are modelled with solid elements representing the trabecular bone and shell elements representing the cortical bone, with an average element side length of 2.5 mm. All rib levels have varying cross-sectional shape and varying cortical bone thickness to match averaged measurements in male ribs (Choi and Kwak 2011), Figure 2 left. The rib cross-sections are defined as elliptical, with height and width dimensions varying along the ribs, Figure 2 right. Both trabecular and cortical bone materials are modelled as isotropic with bilinear material responses (elastic-plastic), with average material parameters based on literature.

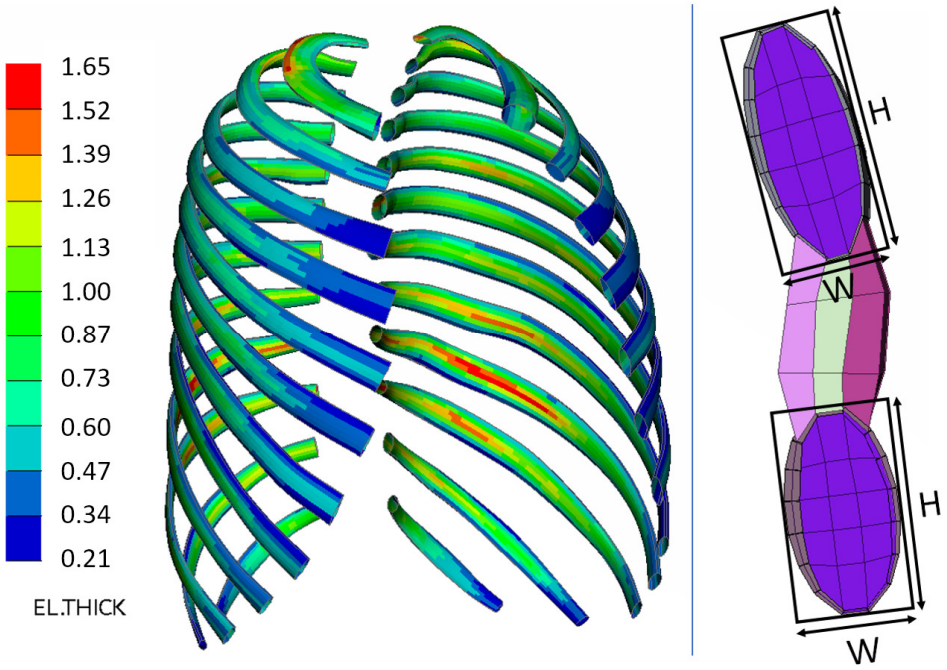


*Figure 2. Left: SHBM rib cortical bone elements, color corresponds to element thickness [mm]. Right: view of the height (H) and width (W) definitions in the elliptical cross-sections of SHBM ribs at level 4 and 5, connected by three layers of solid elements representing intercostal muscle. Here, cortical bone element (gray) thickness is artificially drawn around the shell mid surfaces.*

## 2.3 Statistical Methods

The following subsections introduces statistical methods and definitions used within the thesis.

### 2.3.1 Principal Component Analysis

Principal component analysis (PCA) is a statistical method commonly used to reduce the dimensionality of datasets while keeping as much as possible of the variance (Jolliffe 2002). In this thesis, PCA was used to identify ribcage shape variations among a set of average males under Objective IV. Another application of PCA is the statistical human shape models used for parametric HBM morphing. These models are based on 3D descriptions of individual geometry, which consists of hundreds to thousands of 3D points. With a dataset consisting of several sets of homologous 3D points, together describing geometry from several individuals, PCA can be used to identify the trends of variability within this high dimensional data. This is accomplished by principal components (PCs) aligned with the directions of maximum variance in the data. In many cases, a comparatively small number of PCs (i.e., small in comparison to the original number of data points) can be used to describe most of the variance.

PCA is a linear transformation of the data into new, uncorrelated, variables called PCs, and the dimensionality reduction consists in using only the first few PCs to describe the dataset. While PCA is mostly used for high dimensional datasets, a two-dimensional example can demonstrate key features of PCA, Figure 3. In the example dataset the two variables are correlated (i.e., increasing x1 mainly corresponds to increasing x2), Figure 3, left. The PCs of this dataset are indicated by red arrows. The first PC (PC 1) is, by definition, aligned with the direction of maximum variance in the dataset. The second PC (PC 2) is orthogonal to PC 1 and aligned with the direction of second-to-most variance. For higher dimensional datasets, PC 3 would be orthogonal to PCs 1 and 2 and be oriented in the direction of third-to-most variance, and so on for higher order PCs.

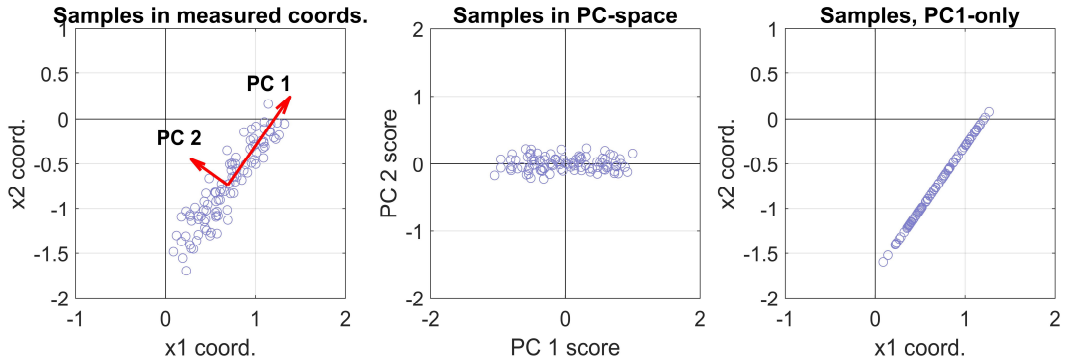


*Figure 3. Left: A dataset of samples in two coordinates. PCs of dataset indicated with red arrows. Middle: The dataset linearly transformed to PC basis. Right: dataset reconstructed using only PC 1.*

In Figure 3, middle panel, the same dataset is plotted using the corresponding PC scores, which are the coordinates in the PC basis. In this view, it is evident that most of the variance is along PC 1. To reduce the dimensionality of this dataset, while keeping as much variance as possible, PC 2 is dropped and only PC 1 is used to describe the dataset. The reduced dimensionality lies in the dropping of higher PCs, which corresponds to directions of less variance. The loss of information becomes

visible if the data is transformed back to the original coordinates using only PC 1 (and the original mean of the dataset), Figure 3, right.

Computation of PCs for a dataset of $n$ samples, each described by $p$ variables, involves subtracting the sample means from the data (centering), and standardizing the samples (important if variables are measured using different units). Next, a centered sample matrix $\boldsymbol{X}$, with $p$ columns and $n$ rows of observations, is created and a sample covariance matrix, $\boldsymbol{S}$, is calculated:

$$\boldsymbol{S} = \frac{1}{n-1}\boldsymbol{X}^T\boldsymbol{X}$$

The PC directions are then the eigenvectors of $\boldsymbol{S}$, with the first PC corresponding to the eigenvector with the largest magnitude eigenvalue, the second PC to the second largest magnitude eigenvalue, and so on (Jolliffe 2002). Routines for performing PCA is commonly available in most software with basic statistics capabilities.

### 2.3.2 Regression modelling

Regression modelling can be used to create a relationship between observed data points and some descriptive predictor variables. For example, regression modelling was used in the construction of the statistical human shape models, where it describes how PC scores relate to e.g., age, sex, height, and BMI. In this thesis it has been used in Objective III to create metamodels (as in models of a model), describing how MHBM rib fracture risk predictions depend on height and weight.

Regression modelling is used to estimate an assumed relationship, $y = f(X)$, between a dependent variable, $y$, and one or several predictor variables: $X = \left[x_1, x_2, \ldots, x_p\right]$. Typically, the dependent variable and the predictors are only known at set of observed points. For a set of $n$ observed points, we then have:

$$(y_1, X_1), (y_2, X_2), \ldots, (y_n, X_n)$$

There exists a plethora of regression models, i.e., methods to build the estimating function (Hastie et al., 2009; Gramacy 2020), but one of the most widely used is linear regression where the function is assumed to take the form (James et al., 2013):

$$y = f(X) = \beta_0 + \beta_1 x_1 + \beta_2 x_2 + \cdots + \beta_p x_p + \varepsilon$$

where it is assumed that the true function has a certain amount of random noise, $\varepsilon$, that is independent of the predictor variables. The noise can correspond to measurement error or hidden (not measured or included) predictor variables. The linear regression estimate of the function is then:

$$\hat{y} = \hat{f}(X) = \hat{\beta}_0 + \hat{\beta}_1 x_1 + \hat{\beta}_2 x_2 + \cdots + \hat{\beta}_p x_p$$

where the $\hat{\beta}_i$ coefficients are commonly found by maximum likelihood estimation (Hastie et al., 2009), or least squares which minimizes the residual sum of squares (RSS) (James et al., 2013):

$$RSS = \sum_i (y_i - \hat{y}_i)^2 = \sum_i \left(y_i - \hat{f}(X_i)\right)^2$$

The difference $y_i - \hat{y}_i$ is called a residual, which is the difference between model prediction and the observed value in the $i^{\text{th}}$ point. As some noise is expected in the observed data, it is generally not expected that all residuals of a regression model are zero, since this can indicate that the regression model follows the noise, rather than the underlying trends in the data.

Note that linear regression is linear in terms of the coefficients, but non-linear predictor combinations can be used, e.g., by choosing $x_2 = x_1^2$, as demonstrated by the example using example data in Figure 4.

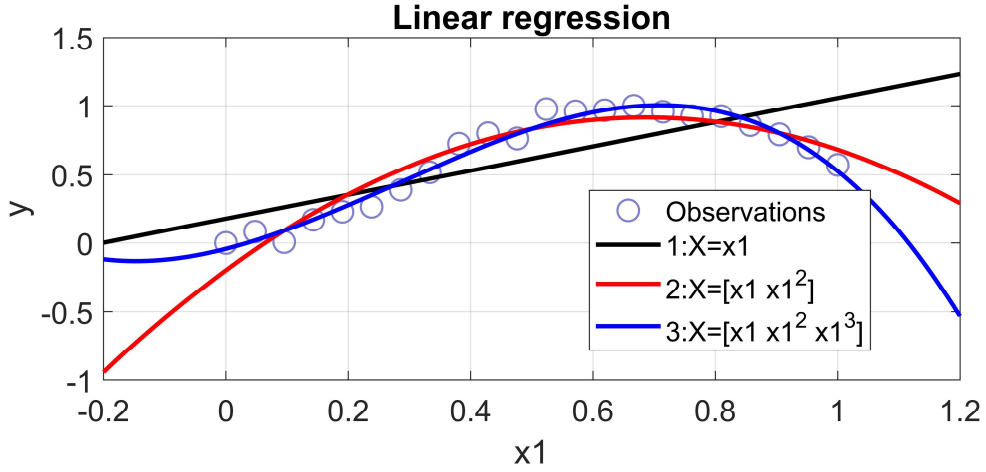


*Figure 4. Examples of linear regression models fitted to the same observations (circles) using polynomial combinations of the predictor variable $x_1$.*

The RSS is an aggregate error measure of how well the regression model fits the observed data. Another common error measure for model fit is the root mean square error (RMSE):

$$RMSE = \sqrt{\frac{\sum_{i=1}^{n}(y_i - \hat{y}_i)^2}{n}}$$

An additional metric that is commonly used to describe how well a model fits observations is the $R^2$ (r-squared) metric, which measures the proportion of variance in the observations of the dependent variable that is explained by the model:

$$R^2 = 1 - \frac{\sum_{i=1}^{n}(y_i - \hat{y}_i)^2}{\sum_{i=1}^{n}(y_i - \bar{y})^2}$$

where $\bar{y}$ is the mean of all $y_i$. A model making predictions that perfectly match all observations will thus have $R^2 = 1$. A model that predicts $\bar{y}$ in all points will have $R^2 = 0$, and models making worse predictions compared to $\bar{y}$ can have $R^2 < 0$.

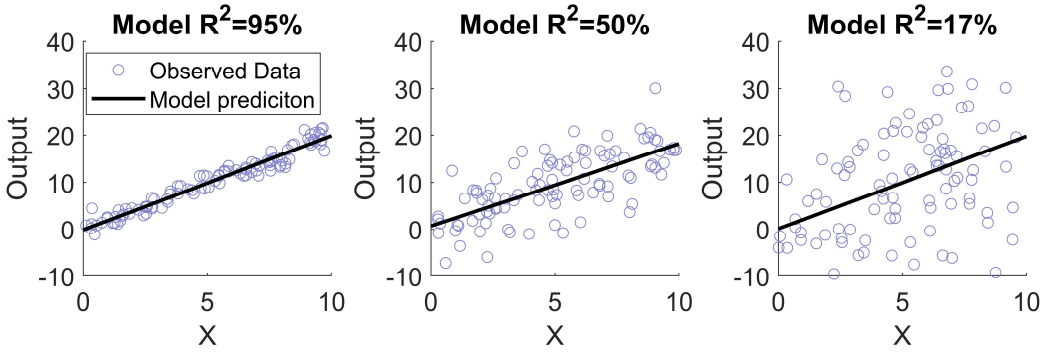


*Figure 5. Three example datasets with corresponding linear regression models fitted, illustrating how $R^2$ relates to variance explained.*

As demonstrated in Figure 5, a high $R^2$-value close to 1, or 100 %, indicates that the model represents the observed data well. As $R^2$ decreases, variance about the model prediction, that is, the residual variance, increases. Thus, models with lower $R^2$ values generally have less predictive accuracy. Common reasons for low $R^2$ values are large measurement noise magnitudes, that too few predictor variables are used, and that the predictor variables are only weakly related to the output variable.

Linear regression is an example of a parametric method. Parametric methods assumes that the function to be estimated follows some functional form or distribution. Non-parametric regression methods, such as e.g., regression forests or Gaussian process regression (Hastie et al., 2009; Gramacy 2020), does not require the form of the estimated function to be pre-specified.

### 2.3.3 Classification and risk functions

Modelling a dependent variable that only can take on a fixed number of values is often referred to as a classification problem. For classification problems, estimated functions predicts the probability that the dependent variable takes on a certain value. A relevant classification problem is creating a risk function, that can be used to predict the probability of injury. In Objective IV, a rib fracture risk function was developed to predict rib fracture risk based on age and rib strain.

A risk function can for example be modelled by logistic regression by assuming the logistic function (one predictor) (James et al., 2013):

$$p(x) = \frac{e^{\beta_0+\beta_1 x}}{1 + e^{\beta_0+\beta_1 x}}$$

Regression coefficient estimates are then obtained through maximum likelihood. Another common way to construct risk functions is to use survival analysis, which models the probability of survival (i.e. not failing) at a certain point in time, or e.g., at a certain force (Kleinbaum and Klein 2012), and the risk is then the probability complement to survival.

To use predictions from a classification or risk function to assign e.g., failure, a threshold level must be chosen, e.g., $p > 0.5$. As the risk function usually includes some uncertainty, there is a risk of misclassification, e.g., predicting failure when there was none (false positive). The proportion of true positives and false positives predicted for a given dataset depends both on the risk function and the chosen threshold value. A common measurement of how well a classifier, or risk function, can classify outcomes correctly is the area under the receiver operator characteristics (ROC) curve (Mandrekar 2010).

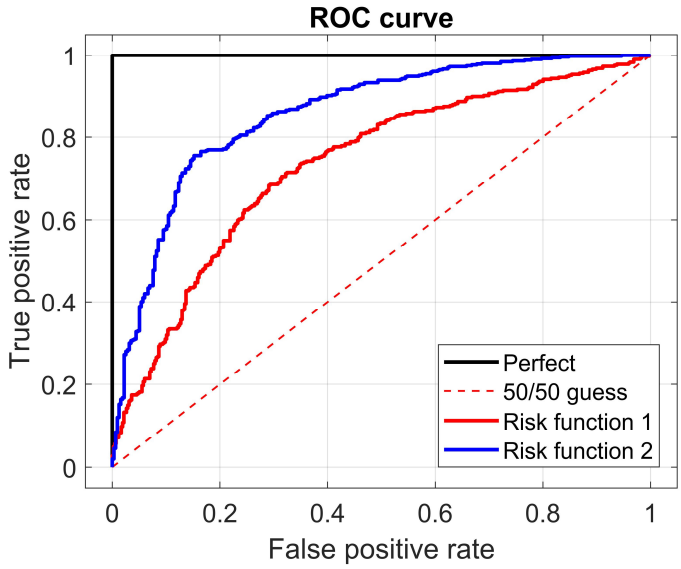


*Figure 6. ROC curves plotted for a perfect classifier, two different example risk functions and 50/50 random guessing.*

To construct the ROC curve, the rate of true positives is plotted against the rate of false positives for all possible threshold values within a dataset containing known

outcomes, see Figure 6. A perfect classifier can obtain a true positive rate of 1 for some ideal threshold value, but also produce false positives for threshold values lower than the ideal. Therefore, the area under the ROC (AUC) for a perfect classifier is 1. For random guessing, the AUC would be 0.5, and a greater area indicates a classifier with improved capability of predicting outcomes. In Objective II, AUC was used to measure the capability of MHBM rib fracture risk predictions to predict rib fracture outcomes.

## 2.4 HBM Validation

As HBM crash simulations are virtual models aiming to represent physical phenomena, it is important that the models are correlated and validated to understand predictive capabilities and correspondence to real-world outcomes before model predictions can be used to make design decisions. In Objective II, MHBM validation was performed by comparison to physical test results.

Validation of an HBM is the process of assessing the model prediction accuracy in comparison to results from one or more reference tests with human subjects (Wismans et al., 2005). For models of humans under potentially injurious conditions, such as high severity crash tests, testing with volunteers is not possible due to ethical considerations. Instead, post mortem human subjects (PMHS), or human cadavers, are commonly used in crash testing to gather kinematic, kinetic and injury outcomes in controlled impact experiments (Yoganandan et al., 2011). Tissue samples, body parts, as well as complete bodies are used, depending on the research question.

In this thesis, MHBM validation was done by comparing MHBM predictions to individual PMHS test results from physical complete body PMHS tests reconstructing occupant impact scenarios. To obtain an objective rating of correlation between MHBM predictions and corresponding subject results, CORA cross correlation rating (Gehre et al., 2009), from the CORA software tool, was used as an objective rating method, using standard CORA control parameters. The CORA cross correlation rating compares the phase, magnitude and shape between a reference test signal and the corresponding model prediction. The correlation rating for a signal ranges from 0 to 1, where 0 corresponds to no correlation and 1 is a perfect correlation.

## 2.5 SHBM Rib Fracture Risk Prediction

A probabilistic strain- and age-based rib fracture risk prediction method (Forman et al., 2012) is used to calculate fracture risk from the SHBM rib strain. This method evaluates the risk of rib fractures in a post-processing step, i.e., rib fracture risk is evaluated after the HBM simulation has terminated. Thus, rib fractures are not explicitly modelled in the SHBM.

There are two parts to the Forman et al. method: an age-adjusted strain-based rib fracture risk function and a probabilistic step where the fracture risks from all 24 ribs are combined into a total risk for the ribcage. The risk function, based on tensile testing with human rib cortical bone, is used to calculate multiple age-specific fracture risks, e.g., one fracture risk per rib given a peak strain value from each rib. With the fracture risks calculated for a specific age, the second part is to combine all fracture risks in a generalized binomial probability model to calculate the combined risk of N total fractures. The risk of N or more fractures is calculated as the probability compliment to the summed risk of obtaining zero to N-1 fractures (Forman et al., 2012).

With SHBM, the maximum value of 1st principal membrane strain from every rib, is used to calculate a risk of two or more fractured ribs (NFR2+) using the Forman et al. (2012) method. The SHBM (v.9) NFR2+ predictions have been validated in PMHS chest impact and sled testing conditions, in accident reconstructions, as well as by comparison to accident database risk from real-world crashes by using stochastic simulations (Pipkorn et al., 2019). Generally, good agreement between the predicted rib fracture risk and the fractures sustained by the PMHS and the occupants in the vehicles in the real-world crashes was obtained.

There are two reasons for targeting prediction of NFR2+ risk. The first is the major risk of severe thoracic trauma and increased mortality risk associated with three or more fractured ribs. Thus, a high NFR2+ risk already represents a crash condition that is not safe which means that measures should be taken to reduce the NFR2+ risk. The second reason is that the probabilistic fracture risk calculation assumes that the rib fracture risks for all 24 ribs are independent. This is generally not true for human ribcages subjected to loading. If a rib fractures during chest loading, its capability to withstand load is reduced, meaning that neighboring ribs need to resist an increased share of the loading, which can lead to an increased risk of subsequent fractured ribs. As rib fracture is not explicitly modelled using the probabilistic method, an increased risk of subsequent rib fractures is not represented. However, in comparison with representing the loss of structural integrity by eroding rib elements exceeding a strain threshold, the probabilistic rib fracture method has even predicted more fractured ribs compared to using element erosion (Guleyupoglu et al., 2018). This indicates that the error from not representing the fracture is likely small for NFR2+ predictions.

## 2.6 Parametric HBM Morphing

This subsection provides a general description of how the statistical shape models are created, how source and target landmarks are used to create interpolating functions performing the morphing, and details in the parametric HBM morphing for SHBM.

Broadly, the statistical shape models for different body parts are created using a similar process (Klein 2015; Klein et al., 2015; Wang et al., 2016; Brynskog et al., 2021; Park et al., 2021) according to; 1) obtain 3D geometry from human subjects. 2) identify homologous landmarks on each individual 3D geometry. 3) fit a template mesh to all individual 3D geometries using the landmarks and a surface alignment algorithm. 4) align fitted template meshes to a common reference position. 5) perform PCA for the nodal coordinates in all fitted template meshes and keep enough PCs to describe a large majority of variance (approx. 90–99 %). 6) build regression models that predicts PC scores based on subject factors. Exceptions for the ribcage shape model are that extra positioning steps, accounting for laterally curved thoracic spines were performed before template mesh fitting, and that two regression models are used to predict ribcage geometry: one for overall ribcage size and one for PCs describing shape variation (Wang et al., 2016). Computed tomography (CT-scan) data were used to obtain individual geometry of bones, and body surface geometry was obtained using external laser scanning. The number of subjects used to obtain landmarks for the different statistical models are shown in Table 1.

The ribcage shape model has landmarks along and around all ribs from the scanned subjects, which means that it can represent both overall shape trends in gross ribcage geometry as well as trends in cross-sectional dimensions as a function of age, sex, height, and BMI. Using these predictors, the ribcage shape model has an $R^2$ of 0.51 (Wang et al., 2016).

*Table 1. Number of females and males used to obtain statistical shape model landmarks.*

| Shape model | Reference | Females | Males |
|---|---|---|---|
| Pelvis | (Brynskog et al., 2021) | 75 | 57 |
| Femur | (Klein et al., 2015) | 36 | 62 |
| Tibia | (Klein 2015) | 28 | 48 |
| Ribcage | (Wang et al., 2016) | 47 | 54 |
| Body surface | (Park et al., 2021) | 73 | 82 |

To morph an HBM to geometrically match targeted age, sex, height, and weight, the corresponding shapes are predicted by the statistical shape models. Node coordinates of corresponding parts in the HBM are morphed to align with their respective statistical shape predictions and are then positioned inside the morphed body surface using known landmarks on bone and body surface geometries (Hwang, Hallman, et al., 2016). The remaining parts of the HBM, not described by a corresponding shape model, are morphed using the shape changes of the nodes in the morphed parts, where their original and morphed configurations provide source and target landmarks, respectively.

The morphing is performed using radial basis function interpolation (Carr et al., 1997; Hwang, Hallman, et al., 2016): Given a set of $n$ known 3D source, $\boldsymbol{x}_{si} = [\, x_{si}\ y_{si}\ z_{si}]$, and corresponding target landmarks, $\boldsymbol{x}_{ti} = [\, x_{ti}\ y_{ti}\ z_{ti}]$, three interpolation functions of the form:

$$s_j(\boldsymbol{x}) = p_j(\boldsymbol{x}) + \sum_{i=1}^{n} w_{ji}\varphi(\|\boldsymbol{x} - \boldsymbol{x_i}\|)\,, \qquad j \in \{x, y, z\}$$

satisfying interpolation conditions:

$$s_x(\boldsymbol{x}_{si}) = x_{ti},\ s_y(\boldsymbol{x}_{si}) = y_{ti},\ s_z(\boldsymbol{x}_{si}) = z_{ti}$$

are sought, i.e., one interpolation for each of the x, y, and z components of the 3D node coordinates.
Here, $p_j(\boldsymbol{x})$ are low order polynomials, chosen to be: $p_j(\boldsymbol{x}) = a_{j0} + a_{j1}x + a_{j2}y + a_{j3}z$, $\|\boldsymbol{x_i} - \boldsymbol{x_j}\| = r_{ij}$ is the Euclidean distance between $\boldsymbol{x_i}$ and $\boldsymbol{x_j}$, and the thin plate spline function is chosen as the radial basis function $\varphi(r) = r^2 log(r)$ (Hwang, Hallman, et al., 2016). Further, orthogonality conditions are applied:

$$\sum_{i}^{n} w_{ji} = 0, \sum_{i}^{n} w_{ji}\boldsymbol{x}_i = \boldsymbol{0}$$

The above can be assembled to matrix form (Hwang, Hu, et al., 2016):

$$\begin{bmatrix} \boldsymbol{A} + \lambda \boldsymbol{I} & \boldsymbol{B} \\ \boldsymbol{B}^T & \boldsymbol{0} \end{bmatrix} \begin{bmatrix} \boldsymbol{w} \\ \boldsymbol{a} \end{bmatrix} = \begin{bmatrix} \boldsymbol{T} \\ \boldsymbol{0} \end{bmatrix}$$

where $\boldsymbol{A}$ is an $n$-by-$n$ matrix with $A_{ij} = \varphi(r_{ij})$, $\lambda$ is a smoothing constant, $\boldsymbol{I}$ is the identity matrix, $\boldsymbol{B} = \begin{bmatrix} 1 & x_{s1} & y_{s1} & z_{s1} \\ \vdots & \vdots & \vdots & \vdots \\ 1 & x_{sn} & y_{sn} & z_{sn} \end{bmatrix}$ is n-by-4, $\boldsymbol{T} = \begin{bmatrix} x_{t1} & y_{t1} & z_{t1} \\ \vdots & \vdots & \vdots \\ x_{tn} & y_{tn} & z_{tn} \end{bmatrix}$ is $n$-by-3, and $\boldsymbol{0}$ are appropriately dimensioned zero matrices.

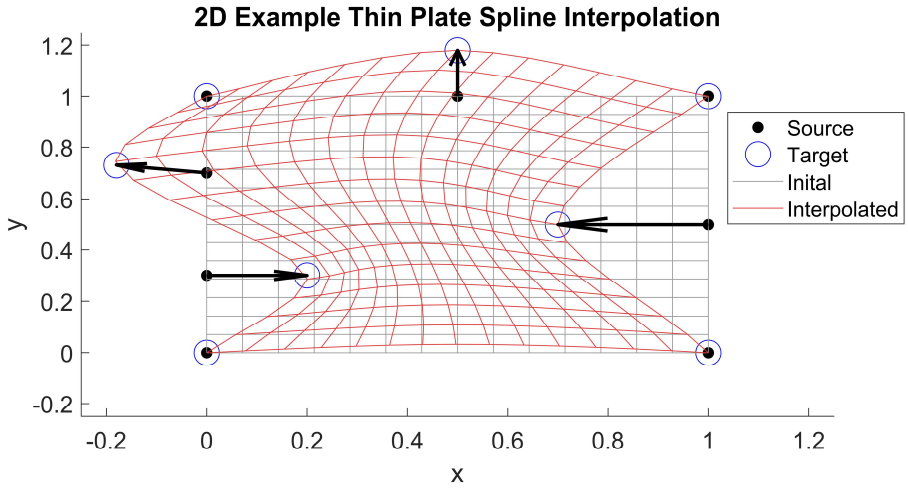


*Figure 7. 2D thin plate spline interpolation used to morph the gray grid into the red grid. Black dots indicate source landmarks, blue circles indicate target landmarks. The arrows indicate the movement from source to target location for displaced target landmarks.*

By solving for the $n$-by-3 weight matrix $\boldsymbol{w}$ and the 4-by-3 coefficient matrix $\boldsymbol{a}$, the three interpolation functions are known. The interpolation functions determined by the source and target landmarks are then used to interpolate new coordinates for other nodes with $\boldsymbol{x}$ as original coordinates. For the parametric HBM morphing, no smoothing ($\lambda = 0$) is used (Hwang, Hallman, et al., 2016). Figure 7 demonstrates a 2D example using two interpolation functions to morph the x and y coordinates of each vertex of the gray grid, into the red grid, based on source and target landmarks.

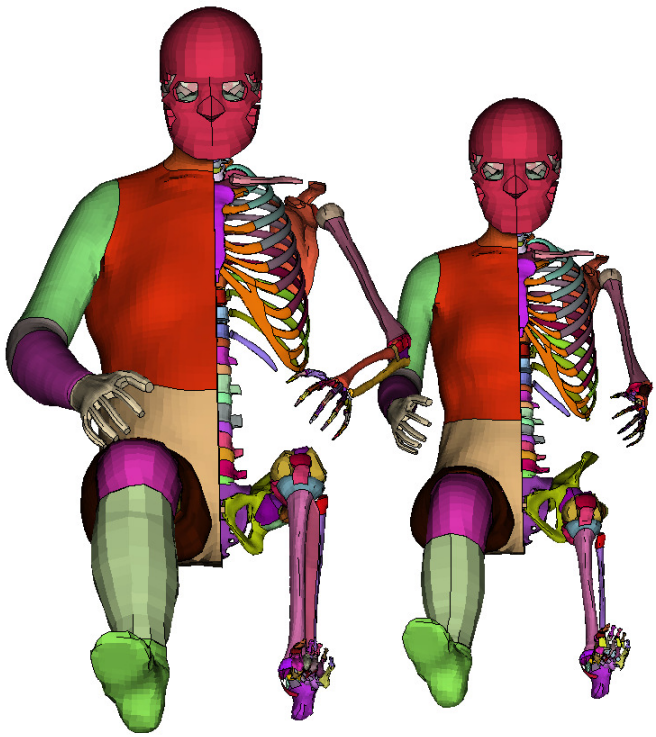

*Figure 8. SHBM as parametrically morphed to (left) male, 189 cm, 127 kg, 35 years, (right) female 151 cm, 52 kg, 35 years. Skin parts hidden to show skeleton.*

For morphing of the SHBM, the parametric morphing method is applied to modify the original nodal coordinates. Additionally, the densities of soft tissues in the torso, arms and legs are uniformly scaled such that the resulting MHBM obtains the target weight. Figure 8 shows the SHBM as morphed to two different morphing targets, representing a large male and a small female. Note that the morphing only adjusts the overall

geometry and mass of the HBM. The parametric HBM morphing method does not adjust material mechanical properties of bone based on e.g., age or sex.

## 2.7 Model Sensitivity Analysis

In Objective IV, the influence on NFR2+ risk from other parameters than those considered in the parametric HBM morphing was investigated. This was done using a variance-based sensitivity analysis, which considers the parameter distributions when calculating parameter sensitivity indices. The resulting sensitivity indices for each parameter corresponds to the average effect on the variance of the output of varying a parameter, for all possible combinations of the other parameters (Sobol' 1990; Saltelli et al., 2008).

Generally, a model output, $Y$, depends on model parameters, $\boldsymbol{x} = [x_1, x_2, \ldots, x_n]$, through some function, $Y = h(\boldsymbol{x})$. Variance-based sensitivity analysis uses the variance decomposition (Sobol' 1990; Saltelli et al., 2008):

$$VAR(Y) = V_Y = \sum_{i}^{n} V_i + \sum_{i}^{n}\sum_{j>i}^{n} V_{ij} + \ldots + V_{ij\ldots n}$$

where $V_i$ is the partial variance of $Y$ due to varying parameter $x_i$, $V_{ij}$, is due to the interaction of $x_i$ and $x_j$ etc. The primary, or first-order, sensitivity index, $S_i = \frac{V_i}{V_Y}$, represents the main average effect contribution (disregarding interactions) of varying $x_i$, for all possible combinations of the other parameters. The second-order index is, $S_{ij} = \frac{V_{ij}}{V_Y}$, and higher order sensitivity indices are defined in the same manner. The total sensitivity index, $S_{Ti}$, accounts for the total contribution to $V_Y$ due to $x_i$, including all higher-order interactions involving $x_i$.

While it is possible to calculate the sensitivity indices analytically for suitable functions, they are generally computed through approximative methods, such as Monte Carlo methods randomly sampling the input parameters many times. However, for crash simulations with FE-HBMs, where a single function evaluation takes hours to compute, Monte Carlo methods are impractical. Therefore an alternative approximative method presented by Zhang and Pandey (2014), based on a multiplicative dimensional reduction method (M-DRM) was used. Here, it is assumed that the model output around a selected input point, called the cut-point: $\boldsymbol{x} = \boldsymbol{c} = [c_1, c_2, \ldots, c_n]$, with $Y_0 = h(c)$, can be decomposed into a set of one-dimensional functions:

$$h(\boldsymbol{x}) \approx Y_0^{1-n} \prod_{i=1}^{n} h_i(x_i, \boldsymbol{c}_{\sim i})$$

where $h_i(x_i, \boldsymbol{c}_{\sim i})$ is a function of $x_i$, and $\boldsymbol{c}_{\sim i}$ is $\boldsymbol{c}$ with $x_i$ excluded. From this assumption it follows that computing $n$ one-dimensional integrals, by e.g., Gaussian quadrature, is sufficient to calculate the sensitivity indices. Thus, for a function of $n$ input parameters and a quadrature rule of $N_{GP}$ integration points, at most $nN_{GP}$ function evaluations are needed (Zhang and Pandey 2014).

# 3 Objective I: Define the Target Population

*Objective I. Determine ranges for parametric HBM morphing targets that are representative of the population of car occupants.*

The approach originally used for specifying the ATD sizes, i.e. they should bracket 90 % of the U.S. population height and weight, was used (Schneider et al., 1983). Therefore, height and weight ranges containing 90 % of the U.S. population, in terms of probability regions respecting the correlation of height and weight were calculated (Brolin et al., 2012). National Health and Nutrition Examination Survey (NHANES) 2013–2016 data was used to calculate 90 % probability regions, using NHANES sample weights. The logarithm of weight was used in the calculations as U.S. NHANES weight distributions have been shown to be right-skewed (Brolin et al., 2020).


*Figure 9. MHBM population target ranges enclosed in thin lines for females (pink) and males (blue). Small pale dots correspond to individual (weighted) samples in NHANES 2013–2016.*

Male and female height and weight ranges of the population to be represented by MHBMs are enclosed by thin lines in Figure 9. For this target population, height ranges are between 146–177 cm (females) and 159–192 cm (males), and weight ranges are 43–130 kg (females) and 54-141 kg (males). These height and weight ranges are for all adult ages.

# 4 Objective II: MHBM Validation

*Objective II. Using the parametric HBM morphing method, develop and validate MHBMs representing the population for prediction of crash kinematics (Paper I) and rib fracture risk.*

The parametric HBM morphing method appears to be a promising method to enable representation of occupant variability in crash safety evaluations with the SHBM. However, before results of such evaluations can be used to guide the design of vehicles and safety systems with reduced injury risk for the population of occupants, it is important that MHBMs are validated to ensure an acceptable level of biofidelity.

## 4.1 Summary of Paper I: Validation of MHBM crash Kinematics

Results in Paper I was obtained using SHBM v.9, later updated to v.10. Updated MHBM validation results, using methods from Paper I for MHBMs based on SHBM v.10 (v.10-MHBMs) follows this summary.

*Table 2. A short test description, Test ID, delta-velocity, and characteristics of PMHS included in each test.*

| Description | Test ID | ΔV [km/h] | Sex [M/F] | Age [Yr] | Ht. [cm] | Wt. [kg] | BMI [kg/m$^2$] |
|---|---|---|---|---|---|---|---|
| Oblique near-side 30°, belt only | 1441 | 35 | M | 60 | 171 | 65 | 22 |
| Frontal, belt only | 1262 | 49 | M | 51 | 175 | 55 | 18 |
| | 1263 | 47 | F | 57 | 165 | 109 | 40 |
| | 1333 | 49 | M | 54 | 189 | 124 | 35 |
| Frontal, belt + airbag | 1761 | 35 | M | 74 | 167 | 66 | 24 |
| Frontal, belt only, constrained legs | s0211 | 30 | F | 57 | 162 | 40 | 15 |
| | s0213 | 30 | F | 65 | 152 | 47 | 20 |
| Oblique far-side 60°, belt only | s0124 | 34 | M | 44 | 182 | 86 | 26 |
| | s0135 | 34 | M | 61 | 178 | 79 | 25 |
| Side impact, thick padding | NBA1004A | 11 | M | 66 | 173 | 79 | 26 |
| | NBA1005A | 11 | M | 51 | 183 | 98 | 29 |
| | NBA1006A | 11 | M | 34 | 188 | 102 | 29 |
| | NBA1006B | 29 | M | 34 | 188 | 102 | 29 |
| | NBA1007A | 11 | M | 87 | 175 | 72 | 24 |
| | NBA1108A | 11 | M | 85 | 178 | 56 | 18 |
| Side impact, thin padding | NBA1109A | 11 | F | 51 | 157 | 68 | 28 |
| | NBA1110A | 11 | F | 80 | 167 | 39 | 14 |
| | NBA1110B | 22 | F | 80 | 167 | 39 | 14 |
| | NBA1213A | 11 | M | 73 | 160 | 53 | 21 |
| | NBA1213B | 22 | M | 73 | 160 | 53 | 21 |
| Side impact, belt + seat airbag | 1701 | 50[1] | F | 61 | 166 | 56 | 20 |
| | 1702 | 50[1] | F | 83 | 155 | 44 | 18 |

[1]Sled test simulates door intrusion and lateral acceleration from a 50 km/h moving deformable barrier to vehicle impact test

For MHBM validation data, PMHS tests performed using male and female subjects of a wide range of anthropometries were gathered from the published literature. In total,

results from 22 tests performed with 19 (7 female) PMHS' were used as reference data for MHBM validation, Table 2. Test configurations included near-side lateral impact, near-side oblique (30°), frontal, and far-side oblique (60°).

For each PMHS, a corresponding MHBM was created by morphing the SHBM (v.9) to geometrically match subject parameters of height, weight, age, and sex using the parametric HBM morphing method. The MHBMs were positioned in models of the test environments using separate positioning simulations, targeted to match the corresponding subject's initial posture. For test cases where a seatbelt was used, a nominal seatbelt webbing model was created, and its initial position followed the seatbelt in the test as close as possible. This nominal seatbelt model, as well as three alternative shoulder belt routings, crossing the sternum at the level of 1$^{st}$, 3$^{rd}$, and 6$^{th}$ rib levels were used to study the influence of shoulder belt routing differences between MHBM and PMHS.

The baseline 50$^{th}$ percentile male SHBM v.9 (B-HBM) was also used to replicate each test with nominal and the additional alternative shoulder belt routings. Targets for B-HBM positioning were obtained by scaling the MHBM positioning targets using the height ratio between B-HBM and respective MHBM.

CORA cross-correlation rating was used to evaluate correlation between HBM (MHBMs and B-HBM) predictions and corresponding, subject specific, test results. For each test, averaged correlation ratings between the set of results from each PMHS test and the corresponding HBM predictions were calculated. The CORA rating and averaging was performed separately for HBM predictions (excursion kinematics, chest deflections) and boundary conditions (seatbelt or impactor forces). The averaging was weighted for each test, with weighting assigned based on peak magnitudes of test results.

To classify goodness of fit between HBM simulations and corresponding test results based on CORA rating, an adapted version of the ISO/TR 9790:1999 biofidelity scale was used: $0 \leq$ unacceptable $< 0.26 \leq$ marginal $< 0.44 \leq$ fair $< 0.65 \leq$ good $< 0.86 \leq$ excellent.

Across frontal, oblique near- and far-side impact tests, CORA ratings ranged from 0.55-0.92 (fair to excellent) for prediction of seatbelt forces and 0.61-0.86 for kinematics. In many cases, correlation ratings were similar for MHBMs and the B-HBM. Exceptions were two frontal impact tests with obese (BMI $\geq$ 30 (World Health Organization 2005)) subjects where correlation to the PMHS kinematics was higher for the obese MHBMs. The obese MHBMs predicted greater magnitude excursions, closer to PMHS levels, than the B-HBM, but still predicted less pelvis excursions than the obese PMHS. Further, for small female PMHS in frontal impact, the MHBMs tended to predict too small forward excursions, while the B-HBM predicted excursion magnitudes greater than the small female PMHS results.

In most cases where shoulder belt routing was varied, MHBM and B-HBM kinematics, seatbelt forces, and resulting CORA ratings were only marginally influenced by initial shoulder belt routing. The exception was one of two 60° far-side impact tests, s0135 Table 2. In this test, all HBMs slipped out of the shoulder belt restraint, except for the MHBM with high initial shoulder belt routing, which resulted in reduced excursion magnitudes for this case.

In lateral impacts, CORA ratings were 0.57–0.88 for impact forces, and kinematic CORA ratings were 0.63–0.89 for lateral spine velocity and 0.18–0.82 for chest deflections. A general trend for all HBMs in the lateral impacts was that greater chest impact forces and smaller chest deflections, compared to corresponding test results, were predicted.

## 4.2 Re-validation of MHBMs based on SHBM v.10

Since Paper I, SHBM was updated to v.10 (Pipkorn et al., 2021; Pipkorn et al., 2023). The parametric HBM morphing method was implemented also for this version. The SHBM updates included a new thoracic soft tissue mesh, including separate modeling of subcutaneous skeletal muscle and adipose tissue, a new average male pelvis geometry and updated modeling of the shoulder joints. The ribcage model from SHBM v.9 was kept.

Kinematic predictions of v.10-MHBMs using nominal seatbelt models were validated using PMHS tests in Table 2, following methods described in Paper I, with one exception. This was an update regarding anterior-posterior chest deflection measurements in tests 1701 and 1702, that were changed to measure chest deflection relative to the spine for PMHS, v.9- and v.10-MHBMs. This was measured as half-depth deflections in Paper I, relative to a reference line spanned between left and right side of PMHS chestbands (lateral nodes at skin of HBM chest). For v.10-MHBMs with updated soft tissues, the reference line was displaced independently of anterior chest deformation. Resulting CORA ratings for v.9- and v.10-MHBMs are shown in Table 3 for frontal and oblique impact scenarios and Table 4 for lateral impacts.

*Table 3. CORA ratings for SHBM v.9- and v.10-based MHBM predictions in frontal and oblique impact scenarios.*

| | Excursion Kinematics | | Seatbelt Forces | |
|---|---|---|---|---|
| Test ID | v.9-MHBM | v.10-MHBM | v.9-MHBM | v.10-MHBM |
| 1441 | 0.83 | 0.80 | 0.87 | 0.87 |
| 1262 | 0.68 | 0.80 | 0.70 | 0.75 |
| 1263 | 0.72 | 0.72 | 0.55 | 0.59 |
| 1333 | 0.75 | 0.75 | 0.76 | 0.81 |
| 1761 | 0.77 | 0.81 | 0.84 | 0.76 |
| s0211 | 0.66 | 0.73 | 0.88 | 0.82 |
| s0213 | 0.67 | 0.77 | 0.81 | 0.88 |
| s0124 | 0.81 | 0.83 | 0.82 | 0.84 |
| s0135 | 0.78 | 0.81 | 0.89 | 0.77 |

In the frontal and oblique impacts, v.10-MHBM kinematic predictions obtained improved CORA ratings for excursion kinematics in tests 1262, s0211 and s0213, Table 3. In test 1262, the v.9-MHBM slipped out of the shoulder belt (for all alternative initial seatbelt routings) and predicted too large forward excursions of the head. The PMHS in this test, as well as the v.10-MHBM did not slip out of the shoulder belt. The resulting v.10-MHBM head excursion prediction was therefore closer to the PMHS result. Tests s0211 and s0213 had small female PMHS' as test subjects, Table 2, and v.9-MHBMs predicted too small forward excursions in these tests. The v.10-MHBMs predicted increased forward excursions, closer to the test results and obtained improved kinematic CORA ratings. For tests 1263 and 1333 with

obese subjects, v.9- and v.10-MHBM kinematic predictions were similar, and the CORA ratings were the same for both versions of MHBMs.

*Table 4. CORA ratings for SHBM v.9- and v.10-based MHBM predictions in lateral impact scenarios.*

| Test ID | Lat. Vel. Kinematics | | Deflections | | Impactor Forces | |
|---|---|---|---|---|---|---|
| | v.9-MHBM | v.10-MHBM | v.9-MHBM | v.10-MHBM | v.9-MHBM | v.10-MHBM |
| NBA1004A | 0.65 | 0.73 | 0.61 | 0.75 | 0.70 | 0.79 |
| NBA1005A | 0.72 | 0.79 | 0.63 | 0.94 | 0.82 | 0.85 |
| NBA1006A | 0.65 | 0.82 | 0.56 | 0.87 | 0.84 | 0.85 |
| NBA1006B | 0.70 | 0.69 | 0.55 | 0.90 | 0.81 | 0.78 |
| NBA1007A | 0.72 | 0.79 | 0.47 | 0.71 | 0.76 | 0.87 |
| NBA1108A | 0.76 | 0.73 | 0.65 | 0.89 | 0.74 | 0.85 |
| NBA1109A | 0.75 | 0.74 | 0.36 | 0.65 | 0.61 | 0.68 |
| NBA1110A | 0.76 | 0.84 | 0.42 | 0.59 | 0.62 | 0.72 |
| NBA1110B | 0.74 | 0.73 | 0.38 | 0.58 | 0.59 | 0.71 |
| NBA1213A | 0.73 | 0.79 | 0.73 | 0.89 | 0.67 | 0.73 |
| NBA1213B | 0.89 | 0.82 | 0.61 | 0.76 | 0.77 | 0.82 |
| | | | | | Seatbelt forces | |
| 1701 | 0.88 | 0.78 | 0.24* | 0.43* | 0.85 | 0.74 |
| 1702 | 0.83 | 0.77 | 0.31* | 0.36* | 0.73 | 0.75 |

*Normalized anterior-posterior chest deflection measurements updated to be relative to spine for PMHS and v.9- as well as v.10-MHBMs

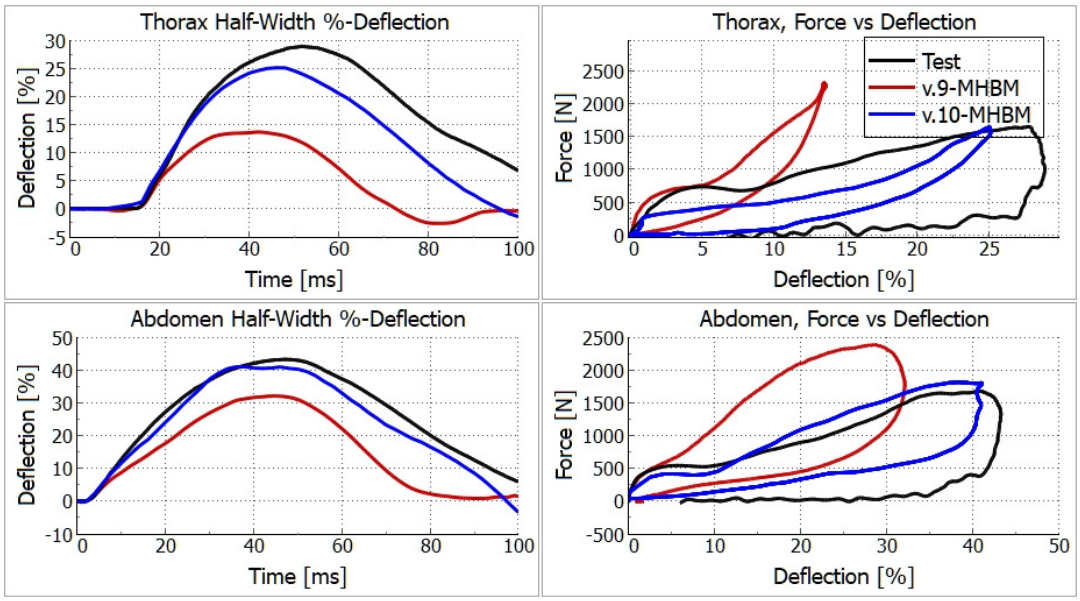


*Figure 10. Left column: Lateral chest deflections measured at the thorax and abdomen levels in test NBA1006A (black), v.9 (red) and v.10-MHBMs (blue). Right column: Force vs. deflection.*

For the lateral impacts, the major difference between v.9- and v.10-MHBMs was improved CORA ratings for chest deflections for v.10-MHBMs, Table 4. Overall, v.10-MHBMs predicted greater deflection and lower impact force magnitudes in the chest region compared to v.9-MHBMs, as demonstrated by deflection and force

results from test NBA1006A in Figure 10. In this test setup, PMHS lateral chest deflection results were reported as percent of half of the initial thoracic lateral width from chestbands at two levels. Impact force results were reported from force transducers mounted behind impactors, each impacting the PMHS in different target regions. In the MHBM simulations, the same measurements, relative to initial MHBM thoracic half-width, were calculated from relative node displacements in locations corresponding to chestband positions on the PMHS. The contact force between each impactor and the MHBM was used for the force results.

For tests 1701 and 1702, v.10-MHBM CORA rating was improved when compared to v.9-MHBM results, but the v.10-MHBM CORA ratings still only received a marginal biofidelity rating, Table 4. The low average chest deflection CORA ratings were mainly due to differences in anterior-posterior deflections between test results and MHBM predictions, see Figure 11 showing chest deflection results from test 1701. In the tests, the chest expanded anteriorly at the xiphoid level (lower end of sternum), seen as negative deflection results in Figure 11, while the v.10-MHBMs predicted a compression of the chest. The reason for this difference in chest deformation behavior is not known. A possible contributing factor can be differences in overall ribcage and torso geometry between the individual test subject and the MHBM torso geometry predicted by statistical body and ribcage shape models in the morphing. In Larsson et al. (2019), a personalized model, created by further morphing the parametrically morphed v.9-MHBM to geometrically match the 1701 subject ribcage (from CT-scan) and torso geometry (chestband shapes) predicted an expansion at the xiphoid chestband, but of smaller magnitude than the test result.

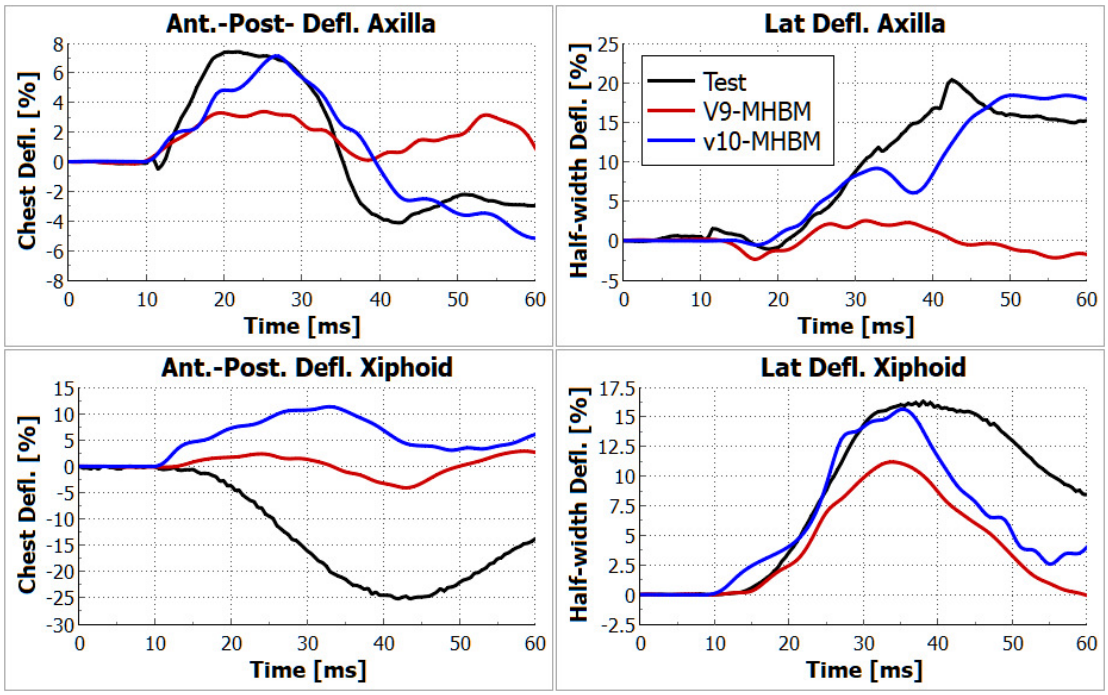


*Figure 11. Normalized chest deflections measured at the axilla (armpit) and xiphoid process (lower end of sternum) levels in test 1701 (black), v.9 (red) and v.10-MHBMs (blue). Left: anterior-posterior deflections. Right: lateral deflections.*

## 4.3 Validation of MHBM Rib Fracture Risk Predictions

For each test replicated using v.9-MHBMs in Paper I, an age-adjusted strain-based NFR2+ risk was calculated using the probabilistic method (Forman et al., 2012). For v.10-MHBMs, NFR2+ risk was calculated using the probabilistic method with the

updated age- and strain-based fracture risk function presented in Objective IV, Paper III. The age of each corresponding PMHS was used in the NFR2+ calculations.

Compared to v.9-MHBM, the v.10-MHBM predicted increased NFR2+ risks in most frontal and oblique tests (i.e., tests ID's in Table 3) and tended to produce slightly lower risk predictions most lateral impacts, Table 5. Overall, both v.9- and v10-MHBM NFR2+ risk predictions appear low when compared to the test outcomes, that often had a substantial number of fractured ribs. Exceptions are v.10-MHBM predictions in tests 1262 and 1263 that were saturated at 100 %, with test outcomes of 10 and 17 fractured ribs, respectively (Table 5).

*Table 5. Test ID, subject height, weight and age, number of fractured ribs (NFR) in the test, v.9- and v.10-MHBM NFR2+ risk predictions for Nominal seatbelts.*

| Test ID | Ht. [cm] | Wt. [kg] | Age [Yr] | Test NFR | v.9-MHBM NFR2+ [%] | v.10-MHBM NFR2+ [%] |
|---|---|---|---|---|---|---|
| 1441 | 171 | 65 | 60 | 10 | 2.0 | 85.4 |
| 1262 | 175 | 55 | 51 | 10 | 92.1 | 100.0 |
| 1263 | 165 | 109 | 57 | 17 | 62.5 | 100.0 |
| 1333 | 189 | 124 | 54 | 7 | 10.9 | 99.4 |
| 1761 | 167 | 66 | 74 | 9 | 0.2 | 18.6 |
| s0211 | 162 | 40 | 57 | 10 | 0.0 | 0.0 |
| s0213 | 152 | 47 | 65 | 4 | 0.0 | 0.3 |
| s0124 | 182 | 86 | 44 | 16* | 5.0 | 64.8 |
| s0135 | 178 | 79 | 61 | 10* | 15.8 | 85.8 |
| NBA1004A | 173 | 79 | 66 | 0 | 0.1 | 0.0 |
| NBA1005A | 183 | 98 | 51 | 0 | 0.0 | 0.0 |
| NBA1006A | 188 | 102 | 34 | 0 | 0.0 | 0.0 |
| NBA1006B | 188 | 102 | 34 | 1 | 9.6 | 0.0 |
| NBA1007A | 175 | 72 | 87 | 2 | 0.1 | 0.0 |
| NBA1108A | 178 | 56 | 85 | 3 | 0.1 | 0.0 |
| NBA1109A | 157 | 68 | 51 | 4 | 1.4 | 0.0 |
| NBA1110A | 167 | 39 | 80 | 1 | 0.5 | 1.7 |
| NBA1110B | 167 | 39 | 80 | 7 | 95.8 | 99.7 |
| NBA1213A | 160 | 53 | 73 | 2 | 1.2 | 0.4 |
| NBA1213B | 160 | 53 | 73 | 4 | 62.3 | 83.4 |
| 1701 | 166 | 56 | 61 | 5 | 0.0 | 0.0 |
| 1702 | 155 | 44 | 83 | 10 | 0.4 | 0.0 |

*Number of rib fractures, assumed to be more than two fractured ribs in AUC calculation

To evaluate the utility of v.9- and v.10-MHBM NFR2+ predictions to classify the presence of two or more fractured ribs in the set of PMHS tests, ROC curves were created, and AUC was calculated. Guidelines for AUC utility by Mandrekar (2010) were used: $0.5 \leq$ no utility $< 0.7 \leq$ acceptable $< 0.8 \leq$ excellent $< 0.9 \leq$ outstanding.

Resulting AUC was 0.71 and 0.76 for v.9- and v.10-MHBM NFR2+ predictions, respectively, indicating acceptable utility for both HBM versions, Figure 12.

Overall, based on comparison to PMHS test results, it is concluded that v.10-MHBMs have good biofidelity for excursion kinematics, fair to good biofidelity for chest deflections, and that v.10-MHBM NFR2+ predictions have acceptable utility for predicting two or more fractured ribs.

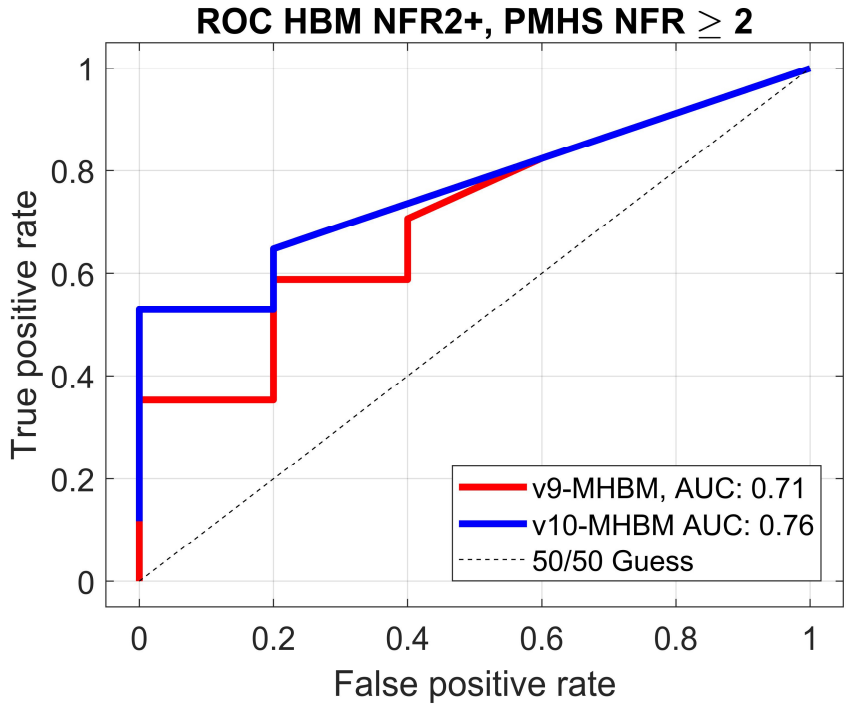


*Figure 12. ROC curves for NFR2+ risk predictions from v.9- (red) and v.10-MHBMs (blue).*

# 5 Objective III: Population Rib Fracture Risk

*Objective III: Develop a method to predict population rib fracture risk, and provide recommendations of how many and which MHBMs to use to represent the population variability in rib fracture risk due to sex, height, and weight variability (Paper II).*

Evaluating the rib fracture risk for the population of occupants through direct computation with MHBMs can become prohibitively time consuming, since a single crash simulation with a detailed FE-HBM can take hours to days to compute. For prediction of MHBM results over the population, a trained metamodel can be used. How many and which MHBM anthropometries that are needed to represent the population variability in rib fracture risk by means of a metamodel were investigated in Paper II.

## 5.1 Summary of Paper II

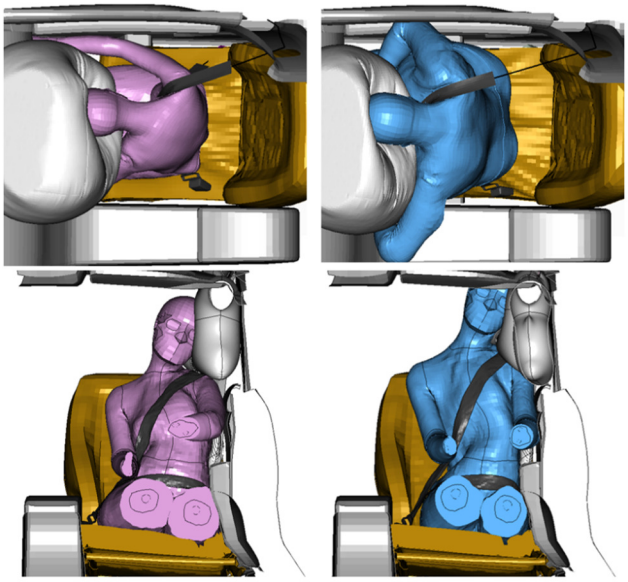

*Figure 13. MHBMs in frontal impact (top row) and near-side impact (bottom row) using generic vehicle interior models. Left column: females. Right column: males*

The method consisted of three main steps. First, metamodel training data representing NFR2+ rib fracture risk outcomes for a population of occupants in frontal and near-side impacts was generated. The occupant population was sampled within the ranges (Objective I, Figure 9) to obtain 200 male and 200 female MHBM height and weight morphing targets. MHBMs were generated by parametric HBM morphing of SHBM v.10, using a fixed age parameter of 45 years. The occupant crash scenarios were modelled using generic vehicle interior models, Figure 13. Resulting frontal impact NFR2+ results ranged from 1 % to 100 %. In the side impact NFR2+ ranged from 0 % to 70 %, Figure 14. Generally, for similar heights and weights, male and female MHBM NFR2+ predictions were different.

Secondly, two regression methods were evaluated for their capability of metamodeling NFR2+ in both accident scenarios: linear regression with second order polynomial terms regularized with least absolute shrinkage and selection operator (LASSO) (Tibshirani 1996) and Gaussian process regression (GPR) (Gramacy 2016). The evaluation consisted of repeatedly measuring metamodel RMSE and $R^2$ for predicting NFR2+ in left-out test points, for metamodels constructed using varying amounts of training data. Here, the resulting RMSE tended to decrease at a high rate with increasing training set sizes, up until approximately 25 randomly selected

MHBMs of each sex. Beyond 25 MHBMs of each sex, the rate of error reduction was reduced. Overall, separate metamodels for each sex constructed using GPR performed best in terms of test set RMSE and $R^2$.

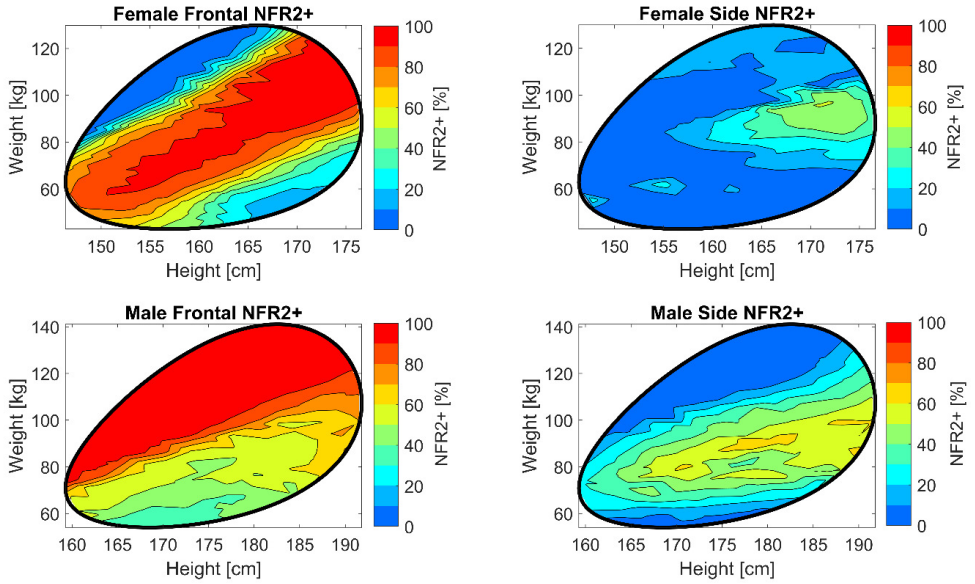


*Figure 14. Contour plots of NFR2+ versus height and weight. The color corresponds to NFR2+ risk in percentage. Top Row: Females. Bottom Row: Males. Left column: Frontal impact. Right column: Near-side impact.*

Third, with separate GPR models for each sex, it was investigated how many, and which MHBMs within the training sample that can be used to represent population NFR2+. Here, "to represent population NFR2+" meant that the metamodel that was constructed using only results from the selected MHBMs had the lowest RMSE error across the entire population sample, averaged over both impact conditions. This was investigated for different subpopulation sizes (up to n=28), starting from three males and three females. For each subpopulation size, individuals were selected by an optimization that minimized an averaged normalized RMSE error, ANRMSE:

$$NRMSE_i = \frac{RMSE_{i,All}}{y_i^{max} - y_i^{min}} \quad \text{(Eq. 1)}$$

$$ANRMSE = 0.5 * NRMSE_{Front} + NRMSE_{Side} \quad \text{(Eq. 2)}$$

Where $RMSE_{i,All}$ was the metamodel RMSE calculated for all available NFR2+ results in the population, and $y_i^{max}$, $y_i^{min}$ were the largest and smallest outputs among the currently evaluated training points.

Resulting GPR models constructed from seven or more selected individuals had population $R^2 > 0.80$ for both males and females in both crashes.
Overall, the results indicate that GPR models constructed using 25 MHBMs of each sex, evenly sampled across their corresponding height and weight regions, can be used to predict NFR2+ for the population in a crash scenario. Further reducing the number of HBMs requires leveraging known effects of height, weight, and sex on NFR2+, which was done in the optimization. The optimization objective, Eq. 2, can be extended to include NFR2+ outcomes from more cars and crashes, which will be needed to identify a family of MHBMs representative of population NFR2+ for all crashes.

# 6 Objective IV: Additional Parameters

*Objective IV: Determine factors, beyond those considered in the parametric HBM morphing method, that influence the rib fracture risk predictions for the population (Papers III and IV).*

While parametric HBM morphing of the SHBM enables the study of how geometrical shape trends, due to height, weight, age, and sex, influence occupant rib fracture risk, there are additional factors that potentially can influence the resulting rib fracture risk predictions.

One such factor is the rib fracture risk function. The Forman et al., (2012) age and strain-based rib fracture risk function was created based on rib failure strain data from twelve, predominantly older, subjects and used age scaling based on age-trends from femoral cortical bone. In Paper III, a new age- and strain-based fracture risk function was developed using recent rib cortical bone experimental results.

Beyond the risk evaluation itself, individual factors, such as rib and ribcage geometry, as well as material properties vary across the population and are often only weakly related to age, height, weight, and sex. With possibly influential variability in several dimensions, there is a need to prioritize which factors to include when population rib fracture risk should be evaluated through HBM simulations. In Paper IV, the SHBM v.10 was parametrized to represent individual variability in 15 factors, and a parametric sensitivity analysis was performed in frontal and near-side lateral impacts to identify the most influential factors.

## 6.1 Summary of Paper III

Rib cortical bone failure strain data from tensile testing performed with samples extracted from 58 PMHS' (31 males 27 females) (Katzenberger et al., 2020) was used to create an age and strain-based rib fracture risk function. Ages of subjects were 17–99 years. It was investigated if age, sex and the interaction of age and sex influenced failure strain. Parametric survival analysis with accelerated failure time was used to create the risk function. Risk was taken as 1-Survival.

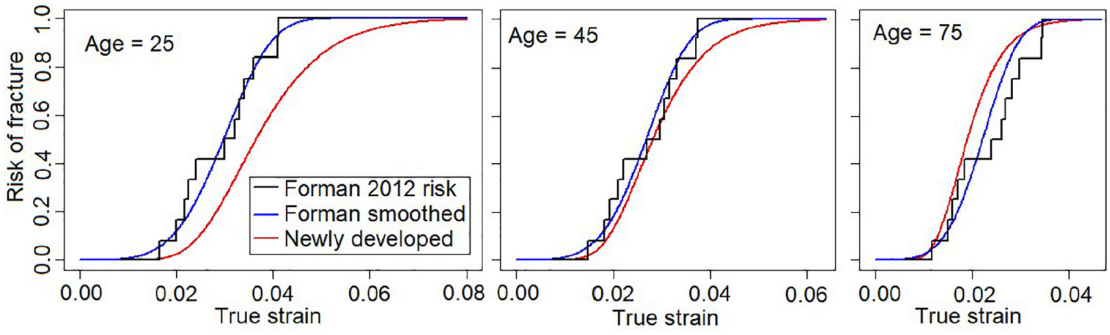


*Figure 15. Newly developed risk function (red) together with Forman et al., 2012, and Forman smoothed for ages (left to right) 25, 45 and 75 years*

Only age influenced failure strain. Thus, age was used as a co-variate in the parametric survival analysis. The log-normal distribution was used to model rib fracture risk as a function of strain and age. The new risk function is plotted vs. strain for three different ages together with the original Forman et al. (2012) and a smooth version of the Forman et al. function (Iraeus and Lindquist 2020) in Figure 15. Compared to previous risk functions, for a given level of rib strain, the new function

predicts lower fracture risk for younger subjects (25 years), similar risk for middle-aged (45 years) and slightly increased risks for older subjects (75 years).

The influence of the new rib fracture risk function on SHBM (v.9) probabilistic NFR2+ rib fracture risk predictions was evaluated by first replacing the original risk function in the Forman et al. (2012) probabilistic calculations. Next, new NFR2+ predictions were calculated using previously generated SHBM (v.9) stochastic simulation results. The stochastic simulations, previously presented in Pipkorn et al. (2019), represented variations of vehicle interior geometry and restraint system design parameters in frontal and near-side crashes of varying delta-velocity. The resulting risk predictions were compared to NFR2+ predictions calculated using the previous risk function and field data estimated risk of NFR2+.

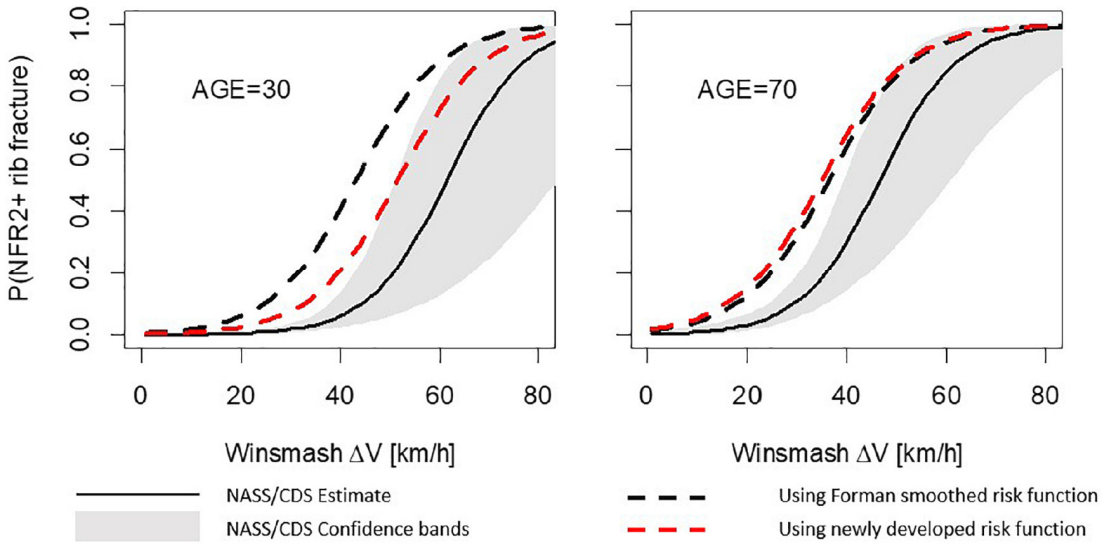


*Figure 16. Near side impact NFR2+ risk versus delta-velocity from stochastic SHBM simulations using the newly developed risk function (red-dashed), smoothed version of Forman et al. 2012 (black-dashed) and field data estimate (NASS/CDS, black solid).*

This resulted in a reduced risk prediction for a given delta-velocity, closer to the field data estimate, for young (30 years) occupants and a slightly increased risk prediction for older occupants (70 years), Figure 16.

In the new rib fracture risk function, the age adjustment corresponds to reducing rib failure strain by 12 % for every 10 years of ageing. This age effect was estimated from experimentally obtained human rib cortical bone failure strain results, and is greater than the 5 % assumed in Forman et al. (2012). As noticed in Figure 16, the main effect of this increased age sensitivity is a reduced risk prediction for younger occupants.

## 6.2 Summary of Paper IV

The SHBM (v.10) was parametrized to represent variability in 15 different factors potentially influencing rib fracture risk. The parameters and parameter ranges were sourced from published literature. As the SHBM represents an average male, male data was used where applicable.

Overall ribcage geometry was varied according to six ribcage shape PCs (Figure 17) identified from a sample of 89 average male subjects in a preliminary study (Larsson et al., 2022). These six PCs together described more than 90 % of variance in ribcage shape geometry in the sample. Also rib cross-sectional height and width was varied.

Variation in these geometrical parameters were achieved by morphing the SHBM using a custom script. Further, the rib cortical bone thickness, assigned as nodal thickness in the rib cortical bone shell elements, was varied.

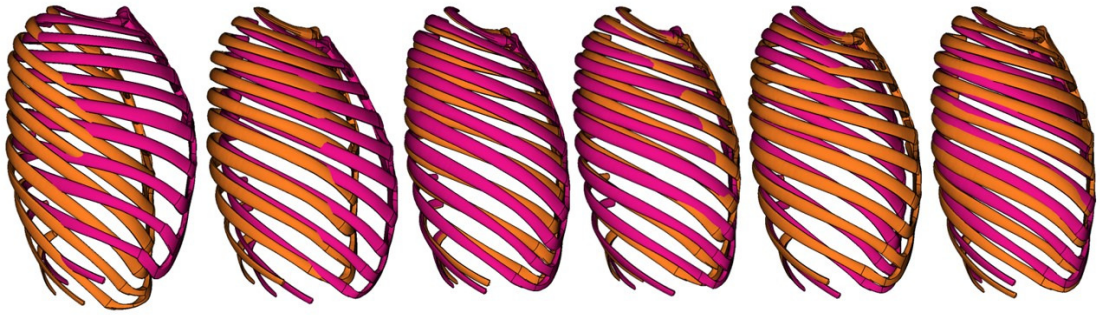

*Figure 17 Ribcage shape variations described by PCs, demonstrated by morphing SHBM ribcage to ± 2 SDs of score of (left to right) PC 1–6.*

Material parameters for material models representing rib cortical and trabecular bone, costal cartilage, intercostal muscle, skeletal muscle, and subcutaneous adipose tissue were varied. For rib cortical bone, rib trabecular bone, and subcutaneous adipose tissue, several material model parameters were co-varied as a function of a single scaling parameter, to represent overall softer and stiffer material responses. This scaling is demonstrated for rib cortical bone in Figure 18, where Young's modulus, yield stress and plastic modulus were scaled simultaneously.

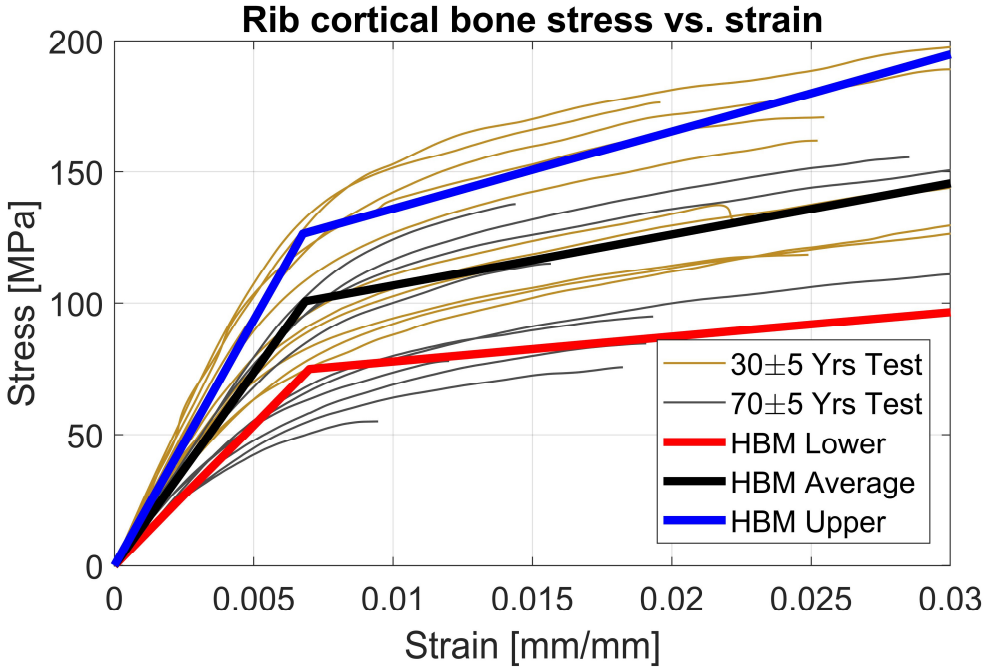


*Figure 18. Ranges of rib cortical bone elasto-plastic isotropic material model parameters illustrated for the parameterized SHBM. Average (black) corresponds to original SHBM material properties, Lower (red) and Upper (blue) denotes the scaling ranges. Thin lines represent tensile test results of human rib cortical bone from younger (30 ± 5 years, yellow) and older (70 ± 5 years, black) (Katzenberger et al.,, 2020).*

Using the parametrized SHBM, variance-based parameter sensitivity analyses for NFR2+ predictions were performed in two occupant impact scenarios, representing a frontal and a near-side lateral impact, respectively. For both impact scenarios the parametrized SHBM was seated as a driver in generic vehicle interior models representing averaged vehicle geometry and generic restraint systems. The variance-

based sensitivity analysis was conducted using an approximative method (Zhang and Pandey 2014), and three parameter sensitivity indices: $S_i$, $S_{ij}$, and $S_{Ti}$ were calculated.

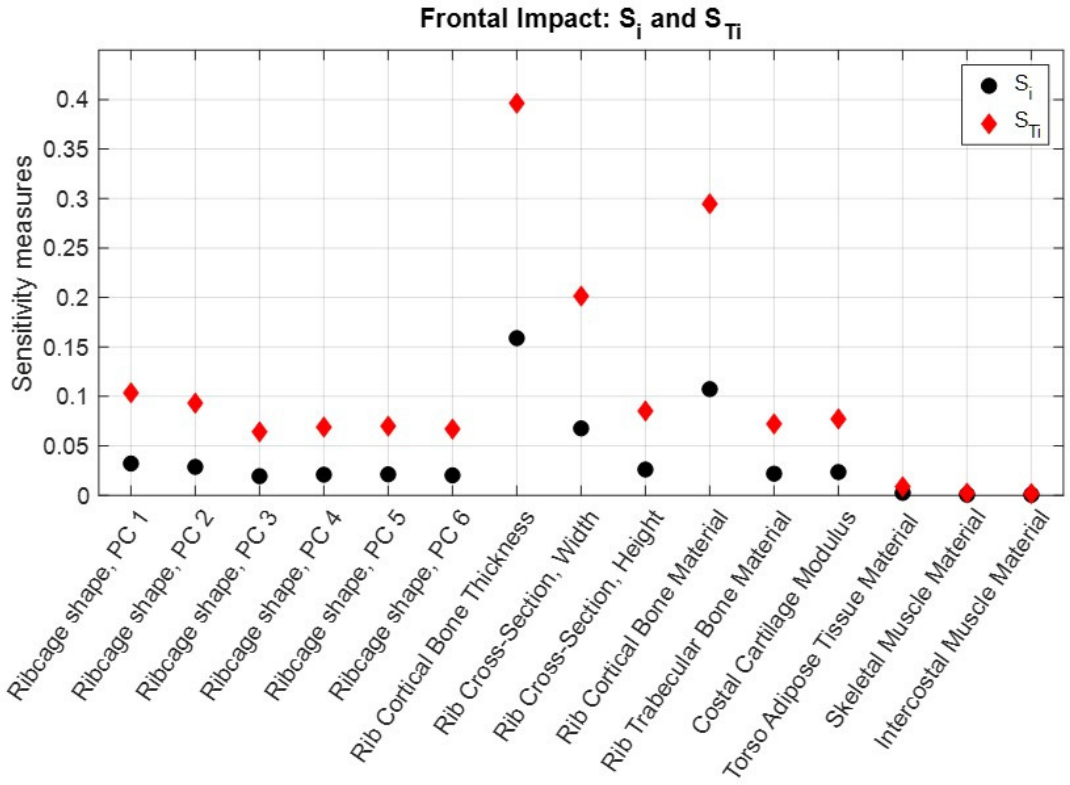


*Figure 19. Frontal impact NFR2+ first-order sensitivity indices $S_i$, (black dots) and total sensitivity indices, $S_{Ti}$, (red diamonds) calculated for each parameter.*

Resulting frontal impact sensitivity indices, $S_i$ and $S_{Ti}$, as well as names for all 15 varied parameters are shown in Figure 19. Based on first order and total sensitivity indices, the same three parameters were identified as being the most influential in both impact conditions. These parameters were rib cortical bone thickness, rib cross-sectional width, and rib cortical bone material parameters, see Figure 19. Based on the total sensitivity index for rib cortical bone thickness, 40 % of the total variability in NFR2+ risk can be attributed to the population variability in cortical bone thickness, due to its first order effect and its interaction effects with other parameters. The second order indices, $S_{ij}$, showed similar interaction effect magnitudes for all parameters in both impacts, and the most substantial interaction effects were, in order: cortical bone thickness and cortical bone material, cortical bone thickness and rib cross-sectional width, and rib cross-sectional width and cortical bone material stiffness. For all remaining parameters, each parameters top three interaction effects were with rib cortical bone thickness, rib cortical bone material stiffness, and rib cross-sectional width.

# 7 Discussion and Future Work

With the overall aim of enabling the assessment of kinematics and rib fracture risk predictions for the population of occupants, the research performed for this thesis has focused on four main objectives. These objectives are: define the target population, MHBM validation, population rib fracture risk prediction, and additional parameters.

## 7.1 Definition of target population

Within the first objective a definition of a population was determined. This population definition includes 90 % of U.S. males and females in terms of height and weight ranges. A population definition consisting of male and female height and weight ranges is suitable to be used in conjunction with the parametric HBM morphing method that uses sex, height, weight, and age as input parameters to create MHBM versions to represent various adult occupants of all ages.

The U.S. population was chosen both because that population has previously been used as the standard population for crash safety evaluation, through the ATD sizes, but also for the open availability of detailed population data through the NHANES program. While similar data from the general population in other countries is, as far as the author is aware, not publicly available, hindering a direct comparison, the ranges obtained from the U.S. population are likely to accommodate a majority of occupants also from other countries. In Table 6, the limits of heights and weights in the MHBM population definition are shown with adult $5^{th}$ – $95^{th}$ percentiles of Swedish (Hanson et al., 2009) and Malaysian (Abd Rahman et al., 2018) heights and weights, as northern European and Asian population examples, respectively. Generally, the MHBM population ranges cover, or are close to the $5^{th}$ and $95^{th}$ percentiles of also these populations. Provided with the corresponding male and female height and weight distribution data, a similar population definition with updated ranges can be determined for a specific country or region.

*Table 6. Adult male and female $5^{th}$ and $95^{th}$ percentiles of height and weight in Sweden and Malaysia. Maximums and minimums of male and female MHBM population ranges.*

| | Male ht. [cm] | | Female ht. [cm] | | Male wt. [kg] | | Female wt. [kg] | |
|---|---|---|---|---|---|---|---|---|
| *Percentile* | *$5^{th}$* | *$95^{th}$* | *$5^{th}$* | *$95^{th}$* | *$5^{th}$* | *$95^{th}$* | *$5^{th}$* | *$95^{th}$* |
| Sweden | 167 | 190 | 156 | 179 | 57 | 103 | 50 | 80 |
| Malaysia | 158 | 172 | 144 | 166 | 53 | 95 | 43 | 81 |
| *Limits* | *min* | *max* | *min* | *max* | *min* | *max* | *min* | *max* |
| MHBM population | 159 | 192 | 146 | 177 | 54 | 141 | 43 | 130 |

All vehicle occupants should, as far as possible, have an equal level of protection. Individuals near the edges of the defined height and weight ranges can be considered statistically rare. However, those individuals present a challenge to vehicle safety systems, by representing various extreme combinations of height and weight that can be encountered in the occupant population. It is likely that safety systems that can provide a high level of protection for these occupants will be able to also protect the occupants closer to the centers, representing more common height and weight combinations. Thus, targeting to achieve a high level of safety for all occupants within these defined ranges has the potential to result in safety systems that are robust to most of the variability in height and weight existing among the population of occupants. Limitations with this population definition are, first, that people can differ in many more dimensions than just sex and overall body height and weight. Some of

these differences affects rib fracture injury tolerance and were further explored under Objective IV. Other differences, such as for example sitting height to stature ratio, percent body fat for a given weight, and variations in self-selected seating posture can potentially influence the resulting injury outcome. Exploring such factors in future research may reveal additional important factors to consider in the definition of a population of occupants. Another limitation is the 90 % target itself, which means that one in ten individuals from the U.S. population will be outside the ranges. However, representing occupants beyond the considered ranges will likely require other methods than parametric HBM morphing, which is beyond the scope of this thesis, as such sizes can potentially mean both substantial extrapolation for the statistical shape models, and extreme shape changes for MHBM FE meshes.

## 7.2 Validation of MHBM Kinematic Predictions

MHBMs were compared to subject specific PMHS results representing various ages, heights and weights for both males and females. This way of validating MHBMs has been applied in previous validations of morphed THUMS, GHBMC and SAFER HBMs (Zhang et al., 2017; Larsson et al., 2019; Hwang et al., 2020). A difficulty with validating MHBM models over a large height and weight range is the limited availability of reference test data. Among the tests included for MHBM validation in Paper I, several of the PMHS' tended to have weights close to the lower weight ranges, and only two PMHS' were obese, Figure 20. The reason is that there is a lack of PMHS tests performed with heavier subjects. Thus, more PMHS tests performed using male and female subjects of a wide range of heights and weights are needed to validate HBMs that are representative of the height and weight variability of today's population. The defined population ranges can aid in selection criteria for future PMHS tests where individuals close to the upper edges of weight should be prioritized for inclusion.

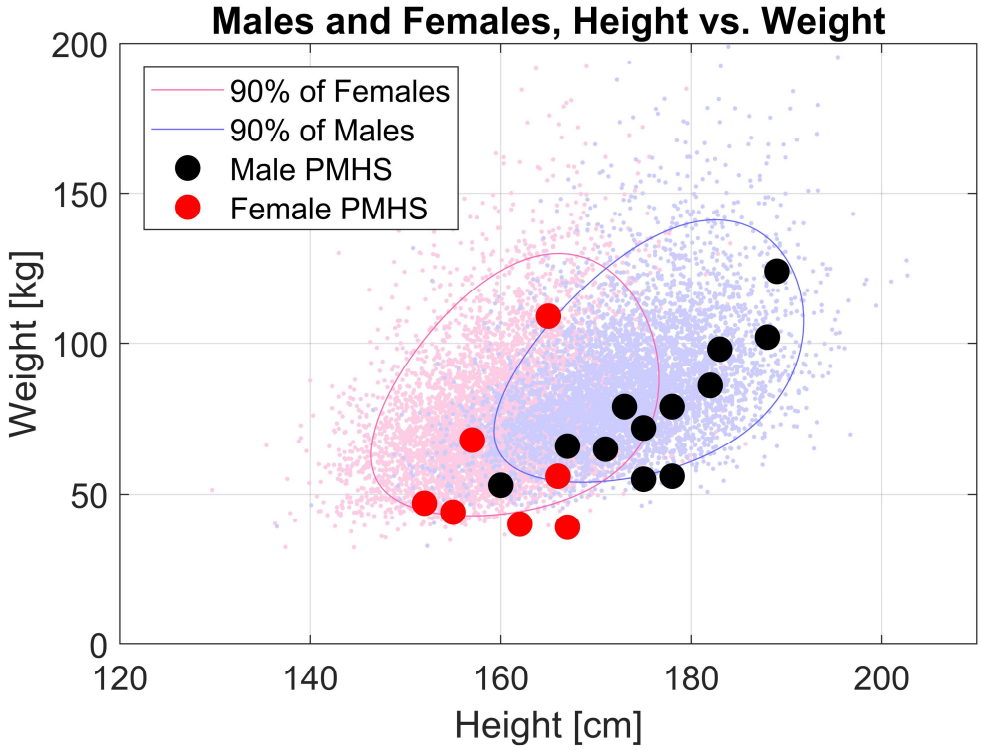


*Figure 20. Height and weight of female (red) and male (black) subjects used for MHBM validation relative to the defined population ranges.*

In addition to sex, height, weight, and age variability, the PMHS tests included for validation data represented variations in impact scenarios and restraint system

settings. A mix of impact configurations adds robustness to the biofidelity evaluation of MHBMs. However, a drawback with using a mix of impact configurations and restraint systems is that it becomes difficult to identify general trends in MHBM predictions with respect to the morphing parameters across the impact configurations, because both boundary conditions and MHBM morphing target parameters change. Therefore, MHBM predictions are influenced both by the morphing as well as by the boundary conditions. Several repeated PMHS tests, representing a wide range of subject sizes within a single test configuration will facilitate correlation analysis as a function of morphing parameters, which can reveal potential limitations of MHBMs.

Additionally, among the included reference tests, different test setups recorded different sets of test results, which further hindered comparison across test configurations. To overcome this issue, a test average CORA rating was used as an overall measure of MHBM correlation. The averaging was weighted towards the test signals with the largest magnitude. This was a way of adjusting for boundary conditions and differences in recorded results across configurations, in that the major force and kinematic PMHS results in each test, irrespective of boundary conditions, had the greatest influence in the final correlation rating.

In most of the evaluated cases, both SHBM v.9-MHBMs (Paper I) and v.10-MHBMs obtained good biofidelity correlation ratings for kinematics. However, some limitations in MHBM predictions were identified. For lateral chest deflections in side impacts, v.9-MHBMs consistently predicted too small deflection magnitudes, whereas v.10-MHBMs predicted larger chest deflections, closer to PMHS results and obtained improved CORA ratings in these cases. As the overall geometry, as well as ribcage models were the same in both versions, this improvement is likely due to the updated material modelling of adipose and muscle tissue in SHBM v.10. For two obese subjects in frontal impact, v.9-MHBMs obtained improved correlation ratings when compared to the, non-morphed baseline SHBM v.9, due to predicting increased forward excursions, closer to the PMHS results. However, the obese v.9-MHBMs still predicted smaller forward excursions of the pelvis than what was obtained in the PMHS tests. Also v.10-MHBMs predicted too small pelvis forward excursions for the obese subjects, even though soft tissue materials around the hip and abdominal regions were updated, Figure 21.

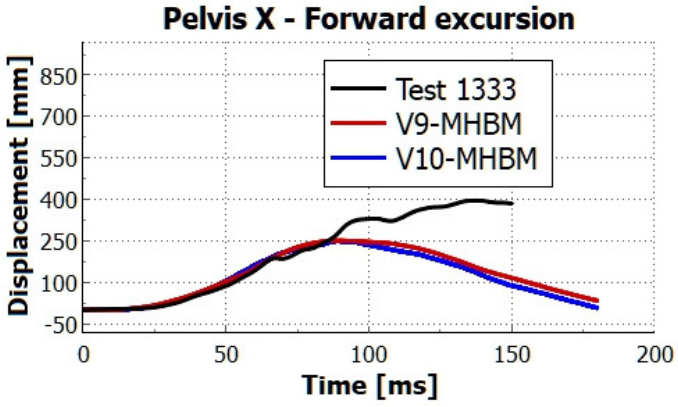


*Figure 21. Pelvis forward excursions in test 1333. Test results (black), v.9- (red) and v.10-MHBM predictions*

For all obese MHBMs it was noted that the lap belt did not penetrate as deep into the abdomen of the MHBMs, as it did for the obese PHMS'. The lack of belt penetration into the abdomen has also been observed for an obese parametrically morphed GHBMC in the same test setup (Gepner et al., 2018). The authors of that study hypothesized that the GHBMC adipose tissue material was too stiff, which is likely

true also for v.9-MHBM material. For v.10-MHBMs the material modelling was improved, as judged by improved chest deflection predictions, but lap belt to abdomen interaction was not influenced when compared to v.9-MHBMs. Another potential reason for poor prediction of lap-belt interaction with obese MHBMs can be that the element quality is reduced when the baseline HBM abdominal mesh is stretched, through morphing, to represent a large volume of adipose tissue. The obese v.9-MHBMs had two solid elements through the thickness of the abdomen, whereas the v.10-MHBMs had three, representing improved element aspect ratios, but this did not influence the results. A third, and likely influential reason is that the parametric morphing method has limited capability to accurately represent the geometry around the hip of higher weight subjects, discussed in the following.

The statistical body shape model used in the morphing is based on laser scanning of seated subject external body geometry (Park et al., 2021). However, for seated subjects of higher weights, the lower abdomen tends to fold over (Janak 2020). The region in the intersection between abdomen and legs, inside the folded abdomen, was not captured by the external laser scans and this region is replaced with a scaled template geometry in the statistical shape model (Park et al., 2021). Resulting parametric MHBMs of higher weights, morphed to fit the statistical body shape model, thus lack the abdominal fold. Janak (2020) developed methods to morph the $50^{th}$ male GHBMC to geometrically match obese PMHS, including the abdominal fold, and found that models with the abdominal fold predicted more realistic interactions with the lap belt. This indicates that representing the abdominal fold can improve MHBM predictions of seat belt interaction and associated pelvis excursions. However, folding over the baseline GHBMC abdominal mesh through morphing alone created negative volume elements and local re-meshing was required (Janak 2020). Therefore, a potential improvement of the modeling of individuals of higher weights in future work can be to create an additional, baseline HBM mesh representing a higher-weight subject with an already existing fold in the abdominal soft tissue. Such a model can potentially be morphed in a simplified way using the statistical body shape model by omitting some landmarks that would correspond to the interior of the fold. Alternatively, detailed morphing can be achieved by obtaining landmarks from medical scanning of seated subjects (Janak 2020), and given a sufficient number of such scans, the abdominal fold geometry can be included in a statistical shape model.

Even though the obese v.10-MHBMs predicted less pelvis forward excursion than the corresponding PMHS, the test condition did not include any instrument panel or similar structure. In a vehicle environment, it is likely that interaction forces between occupant knees or legs and the vehicle interior would reduce the large pelvis excursions observed in the test conditions. Therefore, in a vehicle environment, where excursion is limited, it is likely that obese MHBM kinematic predictions, including pelvis forward excursion, will be more similar to that of a corresponding obese occupant, although the overall force balance between lap belt force and compressive forces through the femurs will differ.

## 7.3 Validation of MHBM Rib Fracture Risk Predictions

For the NFR2+ rib fracture risk validations performed in Objective II, the predicted risk levels from v.9-MHBMs and most v.10-MHBMs appeared low when compared to the number of fractured ribs in each PMHS test, Table 5. As identified under Objective IV, Paper IV, the rib cortical bone thickness, material properties and rib cross-sectional widths have a substantial influence on HBM NFR2+ predictions.

Among these influential factors, only the rib cross-sections are modified to population trends by the parametric morphing, due to the statistical ribcage shape model modifying the overall rib geometry (Wang et al., 2016). While there are statistically significant age trends indicating that both the thickness and material properties of cortical bone are reduced with increasing age, there is also a substantial variability between individuals of similar age, which means that these trends have low predictive capabilities. For example, age and sex can explain ($R^2$) 22–37 % of overall rib cortical bone thickness (Holcombe and Derstine 2022), and age explains 24 % of the material properties Young's modulus and yield stress (Katzenberger et al., 2020). Rib cross-sectional dimensions also varies between individuals (Mohr et al., 2007; Kindig 2009; Holcombe et al., 2019). The large variability means that HBMs representing averaged properties, even if adjusted for age and sex trends, are unlikely to match a particular individual subject, and can therefore predict a mismatching rib fracture risk.

Analysis of frontal impact test results with physical human ribs has identified that individual level parameters, such as age, sex, height and weight are poor predictors for rib stiffness and fracture force in frontal impact experiments with physical human ribs (Agnew et al., 2018). Rib level predictors, utilizing actual rib length and cross-sectional measures performs better and can explain 57 % of stiffness results and, when combined with age, up to 73 % of peak force before rib fracture (Agnew et al., 2018). In the context of validating MHBM rib fracture risk by comparison to individual PMHS rib fracture outcomes, it appears that it would be beneficial for predictive accuracy to not only match overall body size of the MHBM, but also cortical bone thickness distributions, material properties and cross-sectional dimensions of the ribs to the corresponding values in each individual subject.

Such an approach has previously been applied at the rib level, in detailed subject specific modelling of single ribs. Iraeus et al. (2019) modelled mid-level ribs tested in single rib frontal impact experiments. Overall rib geometry and cortical bone thickness distributions of the ribs were obtained from high resolution clinical CT scans (0.164 mm in-plane * 0.625 mm slice thickness). Cortical bone thickness throughout the ribs was obtained with a thickness accuracy of -0.013±0.17 mm, and cortical bone material properties were obtained from tensile testing. The FE mesh size used three hexahedral elements through the cortical bone thickness, resulting in 0.61–1.53 million elements per rib (cf. 3.1–3.4 thousand elements in SHBM mid-level ribs). Generally, the rib model predictions in that study could be divided in two groups: one with good correlations to test results, that predicted experimental forces and high cortical bone strains at the corresponding fracture location, and one with poor correlations. In the poor correlation group, common features were that the subjects had weaker material properties, thinner cortical bone, and higher age (Iraeus et al., 2019). Considering the Iraeus et al. (2019) results, it is indicated that MHBMs would still not be able to predict the rib fracture risk for some of the individuals in the validation reference data, even if subject-specific rib cross-sections, cortical bone thickness, and material properties were implemented in MHBM ribcages.

Rib cortical bone has an inhomogeneous structure. Individuals can for example have varying degrees of intra-cortical porosity (Agnew and Stout 2012), with a trend of increasing porosity with age (Dominguez and Agnew 2016). Pores, or other imperfections, such as microcracks (Agnew et al., 2017), in the cortical bone microstructure, can cause stress concentrations during loading. Iraeus et al. (2019) hypothesized that the ribs in the poor correlation group had greater levels of intracortical porosity. Such microstructural features are too small to be registered, even with the detailed CT-scanning method used to define the rib cortical bone in

Iraeus et al. (2019), and the cortical bone was therefore modelled as a homogenous continuum. It is likely that the continuum modeling assumption for rib cortical bone, applied both in the SHBM ribs and by Iraeus et al. (2019), breaks down as the amount of local imperfections, and associated stress concentrations, increase. Further research, investigating how microstructural features in rib cortical bone affects overall structural properties and fracture risk, as well as modelling strategies incorporating important effects at the level of detail possible in full-body HBMs are needed. This can result in improved rib fracture risk predictions for the part of the population where such effects influence the fracture risk, predominantly older individuals.

For the NFR2+ validations in the current work, is it likely that applying subject specific rib cortical bone material properties, thickness and cross-sectional properties would result in NFR2+ predictions more in line with the observed PMHS rib fracture numbers for some subjects, provided that cortical bone microstructural imperfections are not dominating the fracture mechanisms in the PMHS ribs. As such subject specific data requires a detailed medical imaging protocol and material testing, as well as methods to represent subject specific rib cross-sectional properties and cortical bone thickness distributions along and around the HBM ribs, this is not possible for the current reference set of PMHS tests. Alternatively, as most subjects were 60 years or older, representing known age trends for rib cortical bone material properties and thickness in the SHBM ribs can result in increased NFR2+ predictions that, on average, are more in line with the test outcomes for older subjects (von Kleeck et al., 2022).

Nevertheless, as based on AUC values, both v.9- and v.10-MHBM NFR2+ predictions had acceptable utility for classifying the presence of two or more fractured ribs among the PMHS tests, Figure 12, even though the number of rib fractures in the most vulnerable subjects cannot be predicted. For improved prediction of the most vulnerable subjects, an updated rib cortical bone modeling method, or fracture risk criteria, or both is needed. An improved understanding of rib cortical bone microstructural composition and its effects on material failure on the macroscopic scale is needed to inform future modeling efforts.

## 7.4 Population Rib Fracture Risk

With the capability to evaluate occupant kinematics and rib fracture risk using MHBMs representing a wide range of heights and weights for both males and females, a natural next question is how to assess the rib fracture risk across the defined occupant population. The intention of this assessment is that it enables the development of cars and safety systems with a reduced risk of rib fractures for all occupants. As industrial development of cars and safety systems is performed within time and resource constraints, there is a benefit if such assessments are as time efficient as possible, which can be achieved by reducing the number of different MHBMs used to represent the population, while still maintaining sufficient prediction accuracy.

Within Objective III, Paper II, metamodeling was applied to construct response surfaces of male and female NFR2+ as functions of height and weight in two accident scenarios, to be able to provide recommendations of how many and which MHBMs to use. However, there are some aspects that makes it difficult to provide definitive and general answers.

One aspect is that the crash boundary conditions that the population of MHBMs are subjected to are likely to influence the answer. Examples of boundary conditions that can influence the effects of sex, height, and weight on NFR2+ outcomes include the specifics of each car, such as interior geometry and structural properties, safety systems and their settings, as well as the crash conditions and severity. This was demonstrated by the results from Paper II, where the NFR2+ population outcomes, Figure 14, were different between the frontal and near side impact cases. This means, if the population outcome in each of these crashes should be represented separately, different sets of MHBM sizes would be more suitable for each respective set of boundary conditions, provided a limited number of MHBMs are to be used. Therefore, to enable selecting a set of individuals that are representative beyond a single set of boundary conditions, the optimization in Paper II selected individual MHBMs based on a criterion of average predictive accuracy in both crashes (ANRMSE, Eq. 2). While only representing two boundary conditions is a limited evaluation compared to the number of possible boundary conditions represented by different cars and crash scenarios, the optimization criteria can be expanded to include more boundary conditions. Performing the selection of individuals that minimizes ANRMSE across a broad set of boundary conditions appears to be a promising method to identify a set of individuals that are generally representative of population NFR2+, or other outcomes of interest, due to sex, height and weight variations across the population in future work.

Another aspect is the presence of numerical noise in HBM injury predictions. While HBM crash simulations are deterministic in the sense that re-running the same simulation on the same computer will produce the same results, the numerical calculations involved in the solutions means that small parameter changes spuriously result in larger than expected, i.e., noisy, output changes. One factor that influences the numerical noise is the decomposition performed for multi-core calculations which distributes different parts of the total crash simulation to different computing cores (Östh et al., 2021). As this decomposition depends on which parts are included in the crash simulation, the numerical noise magnitude does not only depend on the specific HBM but can also be different for different boundary conditions. Due to the noise, it is difficult to use simple aggregated model metrics such as RMSE and $R^2$ to define general thresholds for acceptable metamodel accuracy, as such metrics depend on the unknown noise magnitude.

In Paper II, to determine how many HBMs were needed, it was identified at which metamodel training set size the metrics showed diminished improvements with increasing number of training points. The reasoning for this is that substantial reductions in metamodel prediction errors for test points, i.e., points not part of the training data, with increasing training data indicate that the model does not have the capability to predict important trends in the targeted output surface. When increasing the training data instead only yields gradual improvements to the model predictive capabilities, this is an indication that important trends in the output surface are accounted for, and additional training data only serves to locally refine metamodel predictions. One pitfall with this approach is that it is possible to add training data within an already well predicted region, while missing a region that is not yet known to be poorly predicted. In such cases, model error and accuracy measures would remain largely unaffected as training data increase, even though adding points in another region could substantially improve them. In this context, regression methods with capabilities to provide confidence regions about its predictions, such as GPR, can inform about input regions with high predictive uncertainty. Future work with

metamodeling of population injury outputs can provide necessary experience to determine general metric thresholds defining an acceptable metamodel accuracy.

Based on the population NFR2+ outputs and metamodel error trends with increasing training set sizes in Paper II, it was identified that it was possible to construct GPR metamodels representative of the population outcomes with as few as five to ten individuals of each sex. As the individuals were selected through optimization for known outcomes, further studies including variations in vehicle interiors and crash conditions are needed to identify individuals that are generally representative of population NFR2+. To identify the population NFR2+ outcome in other vehicles and crashes it is recommended that at least 25 male and 25 female MHBMs, evenly spread out across the height and weight ranges are used to create a GPR metamodel.

## 7.5 Additional Influential Parameters

Within Objective III, only sex, height, and weight variability were included when modeling the population rib fracture outcomes. However, as investigated in Objective IV, several other parameters can influence NFR2+ predictions.

The reason for not including these parameters in Objective III is that variability in their values is largely independent of the height and weight of an individual. That is, to the best of the knowledge of the author, variability in rib fracture risk caused by the population variability in these parameters exists for both males and females of all heights and weights within the population. This means that for every combination of sex, height, and weight evaluated within the MHBM population, a distribution of NFR2+ outcomes can be computed by repeatedly sampling other parameter values that influence NFR2+ predictions. In doing this, the existing age trends in rib cortical bone thickness and material properties can also be represented. Currently, the NFR2+ risk predicted by MHBMs representing averages of these parameters does not necessarily represent the average of the NFR2+ distribution that would be obtained if the parameter variability was represented. This is because under non-linear circumstances, such as calculating rib fracture risk based on rib strain, Figure 15, models using average parameters does not always predict the average population result (Cook and Robertson 2016).

Therefore, to be able to predict the variable rib fracture risk within the population of occupants though MHBM simulations, it is important that the human variability that influence rib fracture risk predictions, beyond sex, height and weight is represented. The main contribution of Paper IV was to identify that three parameters can represent most of the influence on NFR2+ variability, which greatly simplifies such calculations in future work.

Another way of accounting for the effect of the population variability in the three most influential parameters for NFR2+ without necessarily computing it through repeated crash simulations with an MHBM has been investigated in master thesis work (Solhed 2022). Here, the aim was to create a regression model that uses the rib strains from a HBM simulation with baseline values for the three most influential parameters, and additionally new values for the influential parameters as predictors. This regression model then predicts as output what the resulting rib strains would be, had the new parameter values been represented in the HBM in the crash simulation. The general motivation for such a complementary regression model for rib strain variability is that: while variations in rib cross-sectional width, cortical bone thickness and material properties are highly influential for the strain levels predicted locally in

the ribs, and thus NFR2+ risk, these rib-local variations have little influence on the global HBM response, such as overall kinematics. In Solhed (2022), such a regression model was created for the SHBM v.10 that predicted new rib strain histories across the entire ribcage model. However, remaining tasks for future work lies in generating training data also for MHBMs across the population of occupants. Here, it is important to include a broad range of impact scenarios such that the resulting regression model generalizes well to any impact condition. The benefit of developing such a method is that only baseline MHBM predictions, representing the overall effects of sex, height, and weight to overall chest loading and rib strains in a particular crash, are needed to calculate the distributions of NFR2+ outcomes that are expected due to the population variability.

## 7.6 Applications

With the demonstrated kinematic biofidelity and rib fracture risk prediction capabilities (Objective II), MHBMs based on SHBM can be used as occupant substitutes in the development of vehicles and safety systems. For a particular car and crash scenario, a baseline of population (Objective I) rib fracture risk outcomes due to male and female height and weight variations can be efficiently established using 25 MHBMs of each sex and metamodeling (Objective III). Based on the resulting trends in NFR2+ due to sex, height and weight, alternative safety systems, potentially with features adaptive to occupant characteristics (e.g., reduced seatbelt force limiting levels for lower weight occupants), can be designed and rib fracture risk can be re-evaluated. Reducing the MHBM NFR2+ predictions across the population will likely result in vehicles with a reduced rib fracture risk for all occupants.

In addition to vehicle and safety system manufacturers, crash safety rating and regulatory organizations can use the population of validated MHBMs to define virtual crash test scenarios that motivates development of vehicles with an increased level of safety for all occupants. E.g., Euro NCAP intends to complement its occupant crash protection evaluation with virtual rating tests with HBMs (Euro NCAP 2022). Validated MHBMs along with the population definition and the metamodeling approach, can aid in the selection of challenging virtual vehicle safety evaluation scenarios representing occupant characteristics beyond the traditional ATD sizes.

The findings from Objective IV can be used to improve rib fracture risk prediction from HBMs in several ways. First, the new rib fracture risk function (Paper III) can be used for rib fracture risk predictions with an improved age-sensitivity using any HBM capable of predicting rib cortical bone strain. Examples of applications with THUMS, GHBMC and VIVA+ HBMs exists (Forman et al., 2022; Johansson Sundblad and Wassenius 2022; Ressi et al., 2022). Secondly, the most important factors for HBM rib fracture risk predictions (Paper IV) can be used to prioritize areas of HBM development, such as improving ribcage models, in terms of representing accurate rib geometry and material properties. Additionally, the findings can motivate further research into detailed characterization of rib geometry, rib cortical bone thickness, and material properties, which is crucial input for HBM modelling with an enhanced level of detail. For example, it is not yet established if and how these factors correlate within individuals, which should be considered when the population variability shall be represented in parameterized HBM simulations.

## 7.7 Limitations

Some limitations come from the parametric HBM morphing method used. Beyond limitations in its representation of heavier occupant hip region geometry, it is also

limited in its capability to realistically represent geometry of those skeletal parts that are not described by a statistical shape model, such as the lumbar and cervical spines, the clavicle, and bones of the upper extremities. Similarly, the thickness distribution of muscle and adipose tissue layers is not controlled during morphing. All parts not controlled by a statistical shape model obtain their final morphed shape by interpolation based on how nodes in surrounding parts, that do have a statistical shape model, are deformed. Including statistical shape models for these parts and in particular for the lumbar and cervical spine, whose deformations are involved in overall body kinematic displacements may further improve biofidelity of MHBM kinematic predictions.

For MHBM validations, few PMHS with higher weights were included in the reference tests for MHBM validation, which means that the upper weight ranges in the population definitions are not represented in the validation data. Additional reference PMHS tests performed with higher weight subjects can improve confidence, or identify important limitations, in MHBM predictive capabilities. Furthermore, the validation cases are limited front to side impact cases with subjects in an upright seating posture. No validation of e.g., reclined occupant postures, or rear impact scenarios have been performed.

Additionally, morphing deforms the elements of the baseline HBM mesh, often resulting in degrading element quality, most notably in the skin and subcutaneous soft tissues around the hip and abdomen when modeling obese subjects. While care has been taken to assure that MHBMs are free from major errors, such as initial contact surface intersections, the only strict element quality criteria that has been enforced is Jacobian > 0.2 for solid and shell elements throughout the MHBMs. Even though elements with such low quality have mainly been identified in limited regions, around armpits and the hip for high weight occupants, low quality elements can still influence the overall results. As degraded element quality can reduce the ability of elements to accurately represent deformations, and thus stress and strain, due to external forces, the resulting HBM kinematic and rib fracture risk predictions can be influenced, although the effect of element quality on the predictions in the current work is not known. Further method development towards assuring a high element quality throughout all MHBMs can reduce the uncertainties following uncontrolled element quality.

Further, the rib fracture risk for the most vulnerable, predominantly older, occupants was underestimated. One reason can be that that modelling the rib cortical bone as a homogenous continuum underestimates stress concentrations, or other phenomena from microstructural effects in the cortical bone. Further research utilizing detailed modelling of the cortical bone microstructure can potentially provide guidance into modelling rib fracture risk from such effects at the level of detail possible in full body HBMs.

# 8 Conclusions

With the overall aim to enable the assessment of kinematics and rib fracture risk in crashes for the population of car occupants in virtual crash testing with parametric HBM morphing, this PhD research projects has

- Defined a population target to be represented by MHBMs
- Validated SAFER HBM-based MHBM predictions of kinematics and NFR2+ rib fracture risk across the population of adult vehicle occupants
- Developed a method to predict population NFR2+ risk and provided recommendations of how many and which MHBMs to use to construct GPR-based metamodels that can predict population NFR2+ risk variability due to sex, height, and weight variations within the population
- Constructed a new age and strain-based rib fracture risk function, with the age effect estimated directly from human rib cortical bone testing. This risk function can be used by any HBM capable of predicting strain in the rib cortical bone
- Identified that beyond sex, age, height and weight, the individual variability in rib cortical bone thickness, rib cross-sectional width and rib cortical bone material properties influences NFR2+ risk predictions across the population of occupants

It is concluded that parametric MHBMs based on SAFER HBM, representing geometrical shape trends due to sex, age, height and weight, and rib local individual variability influential for rib fracture risk predictions, can be used to assess kinematics and rib fracture risk for the population of car occupants. Rib fracture risk predictions from parametrically morphed SAFER HBMs have acceptable utility for the population of occupants, but the risk for the most vulnerable, predominantly older occupants, is underestimated.

# 9 References


Abd Rahman NI, Md Dawal SZ, Yusoff N, Mohd Kamil NS. 2018. Anthropometric measurements among four Asian countries in designing sitting and standing workstations. Sādhanā. 43(1):10. doi:10.1007/s12046-017-0768-8.

Agnew AM, Dominguez VM, Sciulli PW, Stout SD. 2017. Variability of in vivo linear microcrack accumulation in the cortex of elderly human ribs. Bone Reports. 6:60–63. doi:10.1016/j.bonr.2017.02.004.

Agnew AM, Murach MM, Dominguez VM, Sreedhar A, Misicka E, Harden A, Bolte IV JH, Kang Y, Stammen J, Moorhouse K. 2018. Sources of Variability in Structural Bending Response of Pediatric and Adult Human Ribs in Dynamic Frontal Impacts. Stapp Car Crash Journal. 62(November 2018):119–192.

Battle CE, Hutchings H, Evans PA. 2012. Risk factors that predict mortality in patients with blunt chest wall trauma: A systematic review and meta-analysis. Injury, Int J Care Injured. 43:8–17. doi:10.1016/j.injury.2011.01.004.

Benhamed A, Ndiaye A, Emond M, Lieutaud T, Boucher V, Gossiome A, Laumon B, Gadegbeku B, Tazarourte K. 2022. Road traffic accident-related thoracic trauma: Epidemiology, injury pattern, outcome, and impact on mortality—A multicenter observational study. PLoS ONE. 17(5):e0268202. doi:10.1371/journal.pone.0268202.

Bose D, Segui-Gomez M, Crandall JR. 2011. Vulnerability of female drivers involved in motor vehicle crashes: An analysis of US population at risk. American Journal of Public Health. 101(12):2368–2373. doi:10.2105/AJPH.2011.300275.

Brolin E, Högberg D, Hanson L. 2012. Description of boundary case methodology for anthropometric diversity consideration. international Journal of Human Factors Modelling and Simulation. 3(2):204–223. doi:10.1504/IJHFMS.2012.051097.

Brolin E, Högberg D, Hanson L. 2020. Skewed Boundary Confidence Ellipses for Anthropometric Data. In: Proceedings of the 6th International Digital Human Modeling Symposium. Skövde, Sweden. p. 18–26.

Brumbelow ML. 2019. Front Crash Injury Risks for Restrained Drivers in Good-rated Vehicles by Age, Impact Configuration, and EDR-based Delta V. In: IRCOBI Conference Proceedings. Florence, Italy.

Brumbelow ML. 2020. Can front crash rating programs using Hybrid III predict real-world thoracic injuries? In: IRCOBI Conference Proceedings. Munich, Germany. p. 679–692.

Brumbelow ML, Jermakian JS. 2022. Injury risks and crashworthiness benefits for females and males: Which differences are physiological? Traffic Injury Prevention. 23(1):11–16. doi:10.1080/15389588.2021.2004312.

Brumbelow ML, Jermakian JS, Arbelaez RA. 2022. Predicting Real-World Thoracic Injury Using THOR and Hybrid III Crash Tests. In: IRCOBI Conference Proceedings. Porto, Portugal. p. 264–287.

Brynskog E, Iraeus J, Reed MP, Davidsson J. 2021. Predicting pelvis geometry using a morphometric model with overall anthropometric variables. Journal of Biomechanics. 126:110633. doi:10.1016/j.jbiomech.2021.110633.

Carr JC, Fright WR, Beatson RK. 1997. Surface interpolation with radial basis functions for medical imaging. IEEE Transactions on Medical Imaging. 16(1):96–107. doi:10.1109/42.552059.

Carter PM, Flannagan CAC, Reed MP, Cunningham RM, Rupp JD. 2014. Comparing the effects of age, BMI and gender on severe injury (AIS 3+) in motor-vehicle crashes. Accident Analysis and Prevention. 72:146–160. doi:10.1016/j.aap.2014.05.024.

Choi H-Y, Kwak D-S. 2011. Morphologic Characteristics of Korean Elderly Rib. J Automotive Safety and Energy. 2(2):122–127.

Cook D, Julias M, Nauman E. 2014. Biological variability in biomechanical engineering research: Significance and meta-analysis of current modeling practices. Journal of Biomechanics. 47(6):1241–1250. doi:10.1016/j.jbiomech.2014.01.040.

Cook DD, Robertson DJ. 2016. The generic modeling fallacy: Average biomechanical models often produce non-average results! Journal of Biomechanics. 49(15):3609–3615. doi:10.1016/j.jbiomech.2016.10.004.

Dogrul BN, Kiliccalan I, Asci ES, Peker SC. 2020. Blunt trauma related chest wall and pulmonary injuries: An overview. Chinese Journal of Traumatology. 23(3):125–138. doi:10.1016/j.cjtee.2020.04.003.

Dominguez VM, Agnew AM. 2016. Examination of Factors Potentially Influencing Osteon Size in the Human Rib. Anatomical Record. 299(3):313–324. doi:10.1002/ar.23305.

Edgecombe L, Sigmon DF, Galuska MA, Angus LD. 2022. Thoracic Trauma. StatPearls Publishing. [accessed 2023 Feb 20]. https://www.ncbi.nlm.nih.gov/books/NBK534843/.

Euro NCAP. 2022. Euro NCAP Vision 2030: a safer future for mobility. Euro NCAP. www.euroncap.com.

Forman J, Kent RW, Mroz K, Pipkorn B, Bostrom O, Segui-Gomez M. 2012. Predicting rib fracture risk with whole-body finite element models: development and preliminary evaluation of a probabilistic analytical framework. In: 56th AAAM Annual Conference. Annals of advances in automotive medicine. Vol. 56. p. 109–124.

Forman J, Kulkarni S, Perez Rapela D, Mukherjee S, Panzer M, Hallman J. 2022. A Method for Thoracic Injury Risk Function Development for Human Body Models. In: IRCOBI Conference Proceedings. Porto, Portugal.

Forman J, Poplin GS, Shaw CG, McMurry TL, Schmidt K, Ash J, Sunnevang C. 2019. Automobile injury trends in the contemporary fleet: Belted occupants in frontal collisions. Traffic Injury Prevention. 20(6):607–612. doi:10.1080/15389588.2019.1630825.

Forman JL, de Dios EDP, Kent RW. 2010. A Pseudo-Elastic Effective Material Property Representation of the Costal Cartilage for Use in Finite Element Models of the Whole Human Body. Traffic Injury Prevention. 11(6):613–622. doi:10.1080/15389588.2010.517254.

Forman JL, McMurry TL. 2018. Nonlinear models of injury risk and implications in intervention targeting for thoracic injury mitigation. Traffic Injury Prevention. 19(sup2):S103–S108. doi:10.1080/15389588.2018.1528356.

Gayzik FS, Moreno DP, Vavalle NA, Rhyne AC, Stitzel JD. 2012. Development of a Full Human Body Finite Element Model for Blunt Injury Prediction Utilizing a Multi-Modality Medical Imaging Protocol. In: 12th International LS-DYNA Users Conference. p. 1–14.

Gayzik FS, Yu MM, Danelson KA, Slice DE, Stitzel JD. 2008. Quantification of age-related shape change of the human rib cage through geometric morphometrics. Journal of Biomechanics. 41(7):1545–1554. doi:10.1016/j.jbiomech.2008.02.006.

Gehre C, Gades H, Wernicke P. 2009. Objective Rating of Signals Using Test and Simulation Responses. Enhanced Safety Vehicle (ESV). Paper Numb:09–0407.

Gramacy RB. 2016. laGP: Large-Scale Spatial Modeling via Local Approximate Gaussian Processes in R. J Stat Soft. 72(1). doi:10.18637/jss.v072.i01. [accessed 2023 Jan 10]. http://www.jstatsoft.org/v72/i01/.

Gramacy RB. 2020. Surrogates: Gaussian process modeling, design, and optimization for the applied sciences. Boca Raton: CRC Press, Taylor & Francis Group.

Guleyupoglu B, Koya B, Barnard R, Gayzik FS. 2018. Failed rib region prediction in a human body model during crash events with precrash braking. Traffic Injury Prevention. 19:S37–S43. doi:10.1080/15389588.2017.1395873.

Hanson L, Sperling L, Gard G, Ipsen S, Olivares Vergara C. 2009. Swedish anthropometrics for product and workplace design. Applied Ergonomics. 40(4):797–806. doi:10.1016/j.apergo.2008.08.007.

Hastie T, Tibshirani R, Friedman J. 2009. The Elements of Statistical Learning. 2nd ed. Springer New York, NY (Springer Series in Statistics).

Holcombe SA, Derstine BA. 2022 Aug 25. Rib cortical bone thickness variation in adults by age and sex. Journal of Anatomy.:joa.13751. doi:10.1111/joa.13751.

Holcombe SA, Kang Y-S, Derstine BA, Wang SC, Agnew AM. 2019. Regional maps of rib cortical bone thickness and cross-sectional geometry. Journal of Anatomy. 235(5):883–891. doi:10.1111/joa.13045.

Holcombe SA, Wang SC, Grotberg JB. 2017. The effect of age and demographics on rib shape. Journal of Anatomy. 231(2):229–247. doi:10.1111/joa.12632.

Hussain A, Burns B. 2022. Anatomy, Thorax, Wall. StatPearls Publishing. [accessed 2023 Feb 18]. https://www.ncbi.nlm.nih.gov/books/NBK535414/.

Hwang E, Hallman J, Klein K, Rupp J, Reed M, Hu J. 2016. Rapid Development of Diverse Human Body Models for Crash Simulations through Mesh Morphing. SAE Technical Paper 2016-01-1491. http://papers.sae.org/2016-01-1491/.

Hwang E, Hu J, Chen C, Klein KF, Miller CS, Reed MP, Rupp JD, Hallman JJ. 2016. Development, Evaluation, and Sensitivity Analysis of Parametric Finite Element Whole-Body Human Models in Side Impacts. Stapp Car Crash Journal. 60(November):473–508. doi:10.4271/2016-22-0014.

Hwang E, Hu J, Reed MP. 2020. Validating diverse human body models against side impact tests with post-mortem human subjects. Journal of Biomechanics. 98:109444–109444.

Iraeus J, Brolin K, Pipkorn B. 2020. Generic finite element models of human ribs, developed and validated for stiffness and strain prediction – To be used in rib fracture risk evaluation for the human population in vehicle crashes. Journal of the Mechanical Behavior of Biomedical Materials. 106(103742). doi:10.1016/j.jmbbm.2020.103742.

Iraeus J, Lindquist M. 2020. Analysis of minimum pulse shape information needed for accurate chest injury prediction in real life frontal crashes. International Journal of Crashworthiness. 26(6):1–8. doi:10.1080/13588265.2020.1769004.

Iraeus J, Lundin L, Storm S, Agnew A, Kang YS, Kemper A, Albert D, Holcombe SA, Pipkorn B. 2019. Detailed subject-specific FE rib modeling for fracture prediction. Traffic Injury Prevention. 20(S2):88–95. doi:10.1080/15389588.2019.1665649.

Iraeus J, Pipkorn B. 2019. Development and Validation of a Generic Finite Element Ribcage to be used for Strain-based Fracture Prediction. In: Proceedings of IRCOBI Conference. Florence, Italy. p. 193–210.

James G, Witten D, Hastie T, Tibshirani R. 2013. An Introduction to Statistical Learning. New York, NY: Springer New York (Springer Texts in Statistics). [accessed 2023 Jan 8]. http://link.springer.com/10.1007/978-1-4614-7138-7.

Janak T. 2020. Personalization of human body models to simulate obese occupants in automotive safety [PhD thesis]. Université de Lyon.

Johansson Sundblad L, Wassenius P. 2022. The human body model VIVA+ in far-side collisions - A validation and evaluation study of HBM usage [Masters Thesis]. [Gothenburg, Sweden]: Chalmers University of Technology.

John J, Klug C, Kranjec M, Svenning E, Iraeus J. 2022. Hello, world! VIVA+: A human body model lineup to evaluate sex-differences in crash protection. Front Bioeng Biotechnol. 10:918904. doi:10.3389/fbioe.2022.918904.

Jolliffe IT. 2002. Principal component analysis. 2nd edition 2002. New York: Springer Science+Business Media, LLC.

Karadayi S, Nadir A, Sahin E, Celik B, Arslan S, Kaptanoglu M. 2011. An analysis of 214 cases of rib fractures. Clinics. 66(3):449–451. doi:10.1590/S1807-59322011000300015.

Katzenberger MJ, Albert DL, Agnew AM, Kemper AR. 2020. Effects of sex, age, and two loading rates on the tensile material properties of human rib cortical bone. Journal of the Mechanical Behavior of Biomedical Materials. 102(103410). doi:10.1016/j.jmbbm.2019.103410.

Kemper AR, Albert DL, Katzenberger MJ, Agnew AA. 2020. Compressive Material Properties of Human Rib Trabecular Bone. In: Proceedings of the Forty-Eighth NHTSA Workshop on Human Subjects for Biomechanical Research.

Kent R, Lee S-H, Darvish K, Wang S, Poster CS, Lange AW, Brede C, Lange D, Matsuoka F. 2005. Structural and material changes in the aging thorax and their role in crash protection for older occupants. Stapp car crash journal. 49(November 2005):231–249.

Kent R, Woods W, Bostrom O. 2008. Fatality Risk and the Presence of Rib Fractures. In: 52nd AAAM Annual Conference. Annals of Advances in Automotive Medicine. Baltimore, USA. p. 10.

Kent RW, Forman JL, Bostrom O. 2010. Is there really a cushion effect: A biomechanical investigation of crash injury mechanisms in the obese. Obesity. 18(4):749–753. doi:10.1038/oby.2009.315.

Kindig M. 2009. Tolerance to Failure and Geometric Influences on the Stiffness of Human Ribs Under Anterior-Posterior Loading. University of Virginia.

von Kleeck BW, Hostetler Z, Fleischmann K, Weaver AA, Gayzik FS. 2022 Jul 21. Age targeted human body models indicate increased thoracic injury risk with aging. Traffic Injury Prevention. 23(S1):S741–S79. doi:10.1080/15389588.2022.2097223.

Klein KF. 2015. Use of Parametric Finite Element Models to Investigate Effects of Occupant Characteristics on Lower-Extremity Injuries in Frontal Crashes [PhD thesis]. University of Michigan.

Klein KF, Hu J, Reed MP, Hoff CN, Rupp JD. 2015. Development and Validation of Statistical Models of Femur Geometry for Use with Parametric Finite Element Models. Annals of Biomedical Engineering. 43(10):2503–2514. doi:10.1007/s10439-015-1307-6.

Kleinbaum DG, Klein M. 2012. Survival Analysis: A Self-Learning Text. New York, NY: Springer New York (Statistics for Biology and Health). [accessed 2023 Feb 5]. http://link.springer.com/10.1007/978-1-4419-6646-9.

Kudzinskas A, Callahan AL. 2022. Anatomy, Thorax. StatPearls Publishing. [accessed 2023 Feb 18]. https://www.ncbi.nlm.nih.gov/books/NBK557710/.

Kullgren A, Stigson H, Axelsson A. 2020. Developments in car crash safety since the 1980s. In: IRCOBI Conference Proceedings. Munich, Germany. p. 86–99.

Larsson K, Pipkorn B, Iraeus J, Bolte IV JH, Agnew AM, Hu J, Reed MP, Sunnevång C. 2019. Evaluation of the Benefits of Parametric Human Body Model Morphing for Prediction of Injury to Elderly Occupants in Side Impact. In: IRCOBI Conference Proceedings. Florence, Italy. p. 150–174.

Larsson K-J, Iraeus J, Pipkorn B, Holcombe SA. 2022. Influence of Individual Ribcage Shape Variability on Occupant Rib Fracture Risk. In: IRCOBI Conference Proceedings. Porto, Portugal. p. 667–684.

Liman ST, Kuzucu A, Tastepe AI, Ulasan GN, Topcu S. 2003. Chest injury due to blunt trauma. European Journal of Cardio-thoracic Surgery. 23.: 374-378

Mandrekar JN. 2010. Receiver Operating Characteristic Curve in Diagnostic Test Assessment. Journal of Thoracic Oncology. 5(9):1315–1316. doi:10.1097/JTO.0b013e3181ec173d.

Mohr M, Abrams E, Engel C, Long WB, Bottlang M. 2007. Geometry of human ribs pertinent to orthopedic chest-wall reconstruction. Journal of Biomechanics. 40(6):1310–1317. doi:10.1016/j.jbiomech.2006.05.017.

NCD Risk Factor Collaboration (NCD-RisC), Di Cesare M, Bentham J, Stevens GA, Zhou B, Danaei G, Lu Y, Bixby H, Cowan MJ, Riley LM, et al. 2016. Trends in adult body-mass index in 200 countries from 1975 to 2014: a pooled analysis of 1698 population-based measurement studies with 19·2 million participants. Lancet (London, England). 387(10026):1377–96. doi:10.1016/S0140-6736(16)30054-X.

Östh J, Pipkorn B, Forsberg J, Iraeus J. 2021. Numerical Reproducibility of Human Body Model Crash Simulations. In: Proceedings of IRCOBI Conference. Online.

Pal C, Tomosaburo O, Vimalathithan K, Jeyabharath M, Muthukumar M, Satheesh N, Narahari S. 2014. Effect of weight, height and BMI on injury outcome in side impact crashes without airbag deployment. Accident Analysis & Prevention. 72:193–209. doi:10.1016/j.aap.2014.06.020.

Park B-KD, Jones MLH, Ebert S, Reed MP. 2021 Oct 21. A parametric modeling of adult body shape in a supported seated posture including effects of age. Ergonomics.:1–9. doi:10.1080/00140139.2021.1992020.

Pipkorn B, Iraeus J, Björklund M, Bunketorp O, Jakobsson L. 2019. Multi-Scale Validation of a Rib Fracture Prediction Method for Human Body Models. In: Proceedings of IRCOBI Conference. Florence, Italy. p. 175–192.

Pipkorn B, Jakobsson L, Iraeus J, Östh J. 2023. THE SAFER HBM – A HUMAN BODY MODEL FOR SEAMLESS INTEGRATED OCCUPANT ANALYSIS FOR ALL ROAD USERS. Enhanced Safety Vehicle (ESV). Paper No. 23-0242. Yokohama, Japan.

Pipkorn B, Östh J, Brynskog E, Larsson E, Rydqvist L, Iraeus J, Perez-Rapela D, Jakobsson L. 2021. Validation of the SAFER Human Body Model Kinematics in Far-Side Impacts. In: Proceedings of IRCOBI Conference. Online. P. 444–476.

Reed MP, Ebert SM, Hallman JJ. 2013. Effects of Driver Characteristics on Seat Belt Fit. Stapp Car Crash Journal. 57(November):43–57. Doi:10.1080/15389588.2012.659363.

Reed MP, Rupp JD. 2013. An anthropometric comparison of current ATDs with the U.S. adult population. Traffic injury prevention. 14(7):703–705. Doi:10.1080/15389588.2012.752819.

Ressi F, Leo C, Klug C, Sinz W. 2022. Protection challenges in seat positions with large rearward adjustment in frontal collisions: An approach using stochastic human body model simulations. Front Future Transp. 3:914481. Doi:10.3389/ffutr.2022.914481.

Ryan A, Knodler M. 2022. Influential crash conditions leading to injury differences experienced by female and male drivers. Journal of Transport & Health. 24:101293. Doi:10.1016/j.jth.2021.101293.

Saltelli A, Ratto M, Andres T, Compolongo F, Cariboni J, Gatelli D, Saisana M, Tarantola S. 2008. Global sensitivity analysis: the primer. Chichester, England ; Hoboken, NJ: John Wiley & Sons Ltd.

Schneider LW, Robbins DH, Pflüg MA, Snyder RG. 1983. Development of Anthropometrically Based Design Specifications for an Advanced Adult Anthropomorphic Dummy Family. Report No.: UMTRI-83-53-1.

Shi X, Cao L, Reed MP, Rupp JD, Hoff CN, Hu J. 2014. A statistical human rib cage geometry model accounting for variations by age, sex, stature and body mass index. Journal of Biomechanics. 47(10):2277–2285. Doi:10.1016/j.jbiomech.2014.04.045.

Shigeta K, Kitagawa Y, Yasuki T. 2009. Development of next generation human FE-model capable of organ injury prediction. Paper No. 09-0111. In: Proceedings of the 21st Enhanced Safety Vehicle (ESV) Conference. Stuttgart, Germany. P. 1–20.

Sirmali M, Türüt H, Topçu S, Gülhan E, Yazici Ü, Kaya S, Taştepe I. 2003. A comprehensive analysis of traumatic rib fractures: morbidity, mortality and management. Eur J Cardiothorac Surg. 24(1):133–138. Doi:10.1016/S1010-7940(03)00256-2.

Sobol' IM. 1990. On sensitivity estimation for nonlinear mathematical models. Matem Mod. 2(1):112–118.

Solhed J. 2022. Applicability of Graph Neural Networks to predict Human variability in Human Body Model Rib Strain Predictions [Master Thesis]. Uppsala Univerity. http://urn.kb.se/resolve?urn=urn:nbn:se:uu:diva-477806.

Tibshirani R. 1996. Regression Shrinkage and Selection Via the Lasso. Journal of the Royal Statistical Society: Series B (Methodological). 58(1):267–288. doi:10.1111/j.2517-6161.1996.tb02080.x.

Vavalle NA, Schoell SL, Weaver AA, Stitzel JD, Gayzik FS. 2014. Application of Radial Basis Function Methods in the Development of a 95th Percentile Male Seated FEA Model. Stapp Car Crash Journal. 58(November):361–384.

Velázquez-Ameijide J, García-Vilana S, Sánchez-Molina D, Martínez-González E, Llumà J, Rebollo-Soria MC, Arregui-Dalmases C. 2021. Influence of anthopometric variables on the mechanical properties of human rib cortical bone. Biomed Phys Eng Express. 7(3):035013. doi:10.1088/2057-1976/abf787.

Wang Y, Cao L, Bai Z, Reed MP, Rupp JD, Hoff CN, Hu J. 2016. A parametric ribcage geometry model accounting for variations among the adult population. Journal of Biomechanics. 49(13):2791–2798. doi:10.1016/j.jbiomech.2016.06.020.

Weaver AA, Schoell SL, Nguyen CM, Lynch SK, Stitzel JD. 2014. Morphometric analysis of variation in the sternum with sex and age: Sternum Morphology with Sex and Age. Journal of Morphology. 275(11):1284–1299. doi:10.1002/jmor.20302.

Weaver AA, Schoell SL, Stitzel JD. 2014. Morphometric analysis of variation in the ribs with age and sex. J Anat. 225(2):246–261. doi:10.1111/joa.12203.

Welsh R, Lenard J. 2001. Male and female car drivers - difference in collision and injury risks. In: 45th AAAM Annual Conference. Annals of Advances in Automotive Medicine. Texas, USA.

Wismans J, Happee R, van Dommelen JAW. 2005. Computational Human Body Models. In: IUTAM Symposium on Impact Biomechanics: From Fundamental Insights to Applications. Vol. 124. Springer. p. 51–58.

World Health Organization. 2005. The SuRF report 2: surveillance of chronic disease risk factors : country-level data and comparable estimates. Geneva: WHO.

World Health Organization. 2018. Global status report on road safety 2018. Geneva Report No.: 9789241565684.

Yang KH, Hu J, White NA, King AI, Chou CC, Prasad P. 2006. Development of Numerical Models for Injury Biomechanics Research: A Review of 50 Years of Publications in the Stapp Car Crash Conference. Stapp Car Crash Journal. 50:429–490. doi:10.4271/2006-22-0017.

Yoganandan N, Stemper BD, Pintar FA, Maiman DJ. 2011. Use of postmortem human subjects to describe injury responses and tolerances. Clinical Anatomy. 24(3):282–293. doi:10.1002/ca.21106.

Zhang K, Cao L, Wang Y, Hwang E, Reed MP, Forman J, Hu J. 2017. Impact Response Comparison Between Parametric Human Models and Postmortem Human Subjects with a Wide Range of Obesity Levels. Obesity. 25(10):1786–1794. doi:10.1002/oby.21947.

Zhang X, Pandey MD. 2014. An effective approximation for variance-based global sensitivity analysis. Reliability Engineering & System Safety. 121:164–174. doi:10.1016/j.ress.2013.07.010.